Chemical Engineering Journal 506 (2025) 159966



Contents lists available at ScienceDirect

Chemical Engineering Journal

journal homepage: www.elsevier.com/locate/cej





CALF-20 obtained by mechanochemical synthesis for temperature swing adsorption CO_2 Capture: A thermodynamic and kinetic study

Federica Raganati [a], Mariangela Bellusci [b], Francesco Leardi [b], Francesca Varsano [b], Paola Ammendola [a,*]

[a] Istituto di Scienze e Tecnologie per l'Energia e la Mobilità Sostenibili (STEMS) - CNR, Piazzale Tecchio 80, 80125 Naples, Italy
[b] ENEA, Casaccia Research Centre, Via Anguillarese 301, 00123, Roma, Italy

ARTICLE INFO

Keywords:
CALF-20
MOFs
Mechanochemistry
Temperature Swing Adsorption (TSA)
Sips isotherm
Pseudo-first/pseudo-second order kinetic models

ABSTRACT

This study examines the potential of CALF-20, a zinc-based metal–organic framework (MOF), synthesized through mechanochemistry, for carbon dioxide (CO_2) capture using temperature swing adsorption (TSA) in post-combustion processes. Unlike conventional methods, mechanochemical synthesis reduces solvent usage and reaction time, aligning with sustainability goals while preserving the structural integrity of CALF-20. This research investigates CALF-20 thermodynamic and kinetic properties, assessing its CO_2 adsorption and desorption performance within a laboratory-scale fixed-bed reactor under various operational temperatures (28–130 °C) and CO_2 concentrations (3–20 % by volume). Key findings reveal that CALF-20 displays promising CO_2 adsorption and desorption efficiency, achieving complete regeneration in each cycle. Sips isotherm analysis demonstrates a high CO_2 adsorption capacity (up to 2.55 mmol g^{-1}) and surface heterogeneity, while isosteric heat of adsorption values confirm a physisorption-driven process. Kinetic analysis shows that the pseudo-first-order model fits the CO_2 adsorption data best, further confirming a primarily physical adsorption mechanism. Additionally, the study demonstrates the stable performance of CALF-20 across ten TSA cycles, underscoring its potential as a viable and sustainable material for CO_2 capture applications.

1. Introduction

Carbon dioxide (CO_2) emissions have become a critical global concern due to their significant contribution to climate change [1,2]. As the world grapples with the urgent need to reduce greenhouse gas emissions, various technologies have emerged to mitigate this problem [3]. Among these, Carbon Capture and Storage (CCS) technologies have gained prominence as a potential solution to reduce CO_2 emissions from industrial sources and power plants [4,5].

Within the realm of CCS, post-combustion capture has emerged as a promising approach, particularly for retrofitting existing facilities [6]. This method involves separating CO_2 from flue gases after the combustion process [7,8]. Among the various techniques for post-combustion capture, adsorption, involving the use of porous materials that can selectively adsorb CO_2 from flue gas streams, has emerged as one of the most promising approaches [9,10]. The efficiency of adsorption processes is attributed to the high surface area and tunable pore structures of these adsorbents, allowing for enhanced CO_2 uptake capacity and selectivity over other flue gas components [11,12]. The appeal of adsorption for post-combustion capture lies in its potential for energy efficiency and operational flexibility, offering several advantages over traditional amine-based absorption processes [13]. These include lower regeneration energy requirements, reduced equipment corrosion, and the ability to handle a wide range of flue gas compositions [9]. Additionally, adsorption technologies can be more easily scaled and retrofitted to existing power plants, making them an attractive option for both new and existing facilities seeking to reduce their carbon emissions [9]. From an engineering perspective, adsorption typically employs two stationary bed reactors. The initial reactor processes the adsorbate-containing feed stream until breakthrough is approaching, which occurs when the adsorbate concentration in the effluent reaches a predetermined threshold (known as the breakthrough value). At this point, the feed is redirected to the second reactor, while the first undergoes regeneration. This regeneration process involves either elevating the temperature (temperature swing adsorption, TSA) or reducing the pressure (pressure swing adsorption, PSA) [14].

* Corresponding author.
E-mail address: paola.ammendola@stems.cnr.it (P. Ammendola).

https://doi.org/10.1016/j.cej.2025.159966
Received 12 November 2024; Received in revised form 24 January 2025; Accepted 24 January 2025
Available online 25 January 2025
1385-8947/© 2025 The Authors. Published by Elsevier B.V. This is an open access article under the CC BY license (http://creativecommons.org/licenses/by/4.0/).

Ongoing research in this field is, therefore, focusing on developing novel advanced adsorbent materials with improved CO_2 capture performance, as well as optimizing process designs to enhance overall system efficiency and reduce operational costs [15].

With reference to the development of innovative adsorbent materials, Metal-Organic Frameworks (MOFs) have emerged as one of the most promising classes of materials for CO_2 adsorption [16]. MOFs, characterized by their crystalline and porous nature, are materials constructed through the coordination of metal ions or clusters with organic ligands. Their high surface area, tunable pore size, and chemical versatility make them excellent candidates for selective CO_2 capture [17]. Among the various MOFs studied for this application, CALF-20 has garnered significant attention in the field of CO_2 capture due to its exceptional properties [18–21]. It is a zinc-based MOF with a well-defined crystalline structure, with a framework composed of layers of 1,2,4-triazoles connected by Zn atoms, with oxalate ions bridging these layers [21–23]. Its structural features, including pore size distribution, have been thoroughly characterized in previous studies, highligtiung a microporous nature [18]. Computational analyses have identified its most probable CO_2 binding site at the center of its pores, further highlighting its suitability for adsorption applications. In addition to its remarkable structural characteristics, CALF-20 exhibits exceptional performance under humid conditions, a critical factor for post-combustion CO_2 capture. Lin et al. [21] demonstrated that CALF-20 maintains its CO_2 adsorption capacity even at relative humidity (RH) levels up to 40 %, with the presence of CO_2 suppressing water sorption, an unusual behavior among physisorbents. This water resistance, combined with its durability over extended cycling (>450,000 cycles under humid conditions), makes CALF-20 a robust material for applications involving moist environments. Similarly, Nguyen et al. (2022) [22] highlighted CALF-20 resistance to water vapor, showing that its adsorption performance remains stable despite exposure to humid conditions. More recently, Nguyen et al. (2024) [24] further explored the competitive adsorption behavior of CO_2 and H_2O on CALF-20, combining thermogravimetric analysis (TGA) with binary dynamic column breakthrough (DCB) experiments. Their findings reveal that at RH < 20 %, the competitive CO_2 loadings are comparable to pure CO_2 loading, indicating that water vapor has minimal impact on CO_2 adsorption despite the physisorptive nature of the material. These studies collectively underscore CALF-20 unique ability to operate effectively in humid environments, further enhancing its potential as a promising material for sustainable and efficient post-combustion CO_2 capture.

Subsequent to the development and selection of sorbent materials, a comprehensive analysis of equilibrium and kinetics is imperative for the design of specific adsorption systems such as TSA and PSA. Equilibrium studies determine maximum adsorption capacity, affinity, and thermodynamics, while kinetic studies reveal adsorption rates, mechanisms, and time to equilibrium. Together, they enable prediction of adsorption behavior, optimization of process parameters, and estimation of adsorbent lifetime [25,26]. This comprehensive approach aids in selecting optimal operating conditions and determining regeneration parameters for both the adsorption (capture) and desorption (sorbent regeneration) phases. An effective adsorbent must, indeed, strike a delicate balance between high equilibrium adsorption capacity and rapid adsorption kinetics [25,26]. As a matter of fact, advanced adsorbent development is increasingly focusing on optimizing both equilibrium and kinetic features through material design, surface modifications, or nanostructure incorporation, ensuring effective CO_2 removal while maintaining operational and economic viability [25,26].

This study presents a comprehensive analysis of the performance of a CALF-20 MOF, synthesized by an unconventional mechanochemical approach, for temperature swing adsorption (TSA) within the context of post-combustion processes. Both CO_2 adsorption and desorption behavior of CALF-20 have been examined in a laboratory-scale fixed bed reactor under various operating conditions. CO_2 adsorption experiments were performed at temperatures ranging from 28 to 130 °C, with CO_2 concentrations varying from 3 to 20 %vol. Desorption was performed at temperatures ranging from 40 to 150 °C under N_2 purge. The results, analyzed using relevant isotherm and kinetic models, provide critical parameters for both adsorption and desorption phases.

2. Experimental

2.1. Materials

In this work the synthesis of CALF-20 is reported using the solvent-assisted mechanical milling method, in which the energy necessary for the formation of the MOF is supplied to the precursor powders through the mechanical impact of balls. A limited amount of solvent was added to the powders which is known to increase the rate of reaction and improve the product crystallinity [27]. Ball-milling technology is gaining increasing interest owing to its low-cost and eco-friendly nature since, as a non–/less-solvent technology, fully fits the demands of environmental sustainability [28,29]. Furthermore, the mechanochemical method has, as its primary objective, the reduction of synthesis times compared to the classical solvothermal synthesis procedure, which has been reported to last 48 h [21]. Indeed, compared to other synthesis techniques such as solvothermal, microwave-assisted, and sonochemical methods, solvent requirements were reduced to 1/10. Additionally, mechanochemistry achieves reaction completion in significantly shorter times (minutes to hours) compared to days for solvothermal methods [30] with consequent energy saving (the developed synthesis consumes approximately 20 % of the energy needed to produce the phase by solvothermal synthesis).

The synthesis was carried out in a Spex Mixer/Mill 8000 using a stainless-steel vial lined with Teflon and 10 mm Zirconia balls with a 1:10 powder/ball ratio starting from zinc oxalate ($C_2H4O_6Zn{\cdot}2H_2O$, Thermo scientific, 99.99 %) and 1,2,4-triazole (C2H3N3, ACROS ORGANICS 99.5 %). The reagents are the same as for solvothermal synthesis [21], used in the same stoichiometric ratio. A small quantity of methanol (J.T. BARKER) was added to the reactive powders to perform Liquid Assisted Grinding (LAG). Liquid-assisted mechanochemistry is in fact much faster than dry milling of precursors. The liquid not only catalyzes the reaction but also functions as a structure-directing and space-filling component, indicating that achieving thorough synthesis necessitates an adequate amount of additive to occupy the MOF pores fully [31,32]. The powder/liquid ratio is defined by the parameter η, which must fall in the range 0–2 μl mg^{-1} [27,33]; in our case it is 0.90 μl mg^{-1}. To study the evolution of the reactants towards the product of interest, the reaction was carried at two different milling times: 30 min (CALF20BM05H) and 1 h (CALF20BM1H). Purification was carried out by washing the material with distilled water five times and collecting the produced powders after centrifugation (10000 rpm-10 min). The synthesis product was left to dry overnight in an oven at 70 °C, and then subsequently activated at 180 °C for 3 h before being characterized.

The crystalline phase of the materials was determined using an Italstructures X-RED 3000 diffractometer with Fe-Kα1 as the radiation source. X-ray measurements were conducted on powders loaded in a glass capillary (1 mm), given the sensitivity of the CALF-20 MOF material to environmental conditions.

The particle size and morphology of the produced powders were observed by Scanning Electron Microspcopy (SEM) using a high-resolution microscope HRSEM LEO130.

The Nitrogen adsorption isotherms at 77 K were performed using a high-resolution Quantachrome Autorsorb iQ instrument. Specific surface area was determined by applying the BET method according to indications reported in [34].

2.2. Experimental apparatus and procedure for CO2 adsorption/desorption tests

CO_2 dynamic adsorption/desorption tests were performed using CALF20BM1H as the sorbent material in a laboratory-scale fixed-bed reactor (inner diameter: 10 mm, column length: 600 mm), as shown in Fig. 1.

The temperature was continuously monitored and controlled using a type-K thermocouple (1 mm diameter) connected to a PID controller, while an electric heating jacket (Tyco Thermal Controls GmbH) was used to maintain the set temperature.

High-purity N_2 and CO_2 gas cylinders (99.995 % vol.) were used to generate the gas mixture for the experiments, with the flow rates accurately adjusted and managed by two mass flow controllers (Brooks 8550S). The adsorption/desorption process was monitored using a continuous gas analyzer with an infrared detector (ABB AO2020, URAS 14). This device measured CO_2 concentration at the reactor exit point during the dynamic adsorption/desorption phase.

2.2.1. Adsorption

Adsorption tests were performed at different temperatures (T = 28, 50, 75, or 130 °C) and CO_2 partial pressures (P_{CO2} = 0.03, 0.05, 0.1, 0.15, and 0.2 atm). The selected experimental conditions, both in terms of temperature and CO_2 partial pressure, are directly relevant for post-combustion CO_2 capture. Indeed, flue gas in typical post-combustion processes is typically released at temperatures of 40–60 °C and CO_2 partial pressures of approximately 0.05–0.2 atm, depending on system design and heat recovery technologies [35,36].

In a standard adsorption test, the sorbent (2 g, equivalent to approximately 5 cm of bed height) underwent a drying and cleaning process, where N_2 is passed through the system at a flow rate of 15 L h^{-1} for 60 min at 180 °C under atmospheric pressure. Following this, in a pre-conditioning phase, the temperature was adjusted to the target adsorption value (28, 50, 75, or 130 °C) while maintaining a continuous flow of N_2 at 15 L h^{-1} through the bed. After reaching the target adsorption temperature, the adsorption process was initiated by introducing a CO_2/N_2 gas mixture (with CO_2 concentrations, C_0, of 3, 5, 10, 15, or 20 % by volume, corresponding to CO_2 partial pressures, P_{CO2}, of 0.03, 0.05, 0.1, 0.15, and 0.2 atm) into the column at a flow rate of 15 L h^{-1}. The breakthrough curves were obtained by continuously monitoring the CO_2 concentration in the outlet stream until the bed became saturated, as indicated by the outlet CO_2 concentration approaching the inlet value.

In each CO_2 adsorption experiment, a breakthrough curve was derived, illustrating the ratio of C/C_o over time, where C refers to the volumetric CO_2 concentration in the outlet stream and C_o represents that in the inlet stream. From these data, the key adsorption parameters were determined through detailed analyses [9,37,38]:

i) q_e – The amount of CO_2 adsorbed per unit mass of adsorbent is calculated by integrating the breakthrough curves according to the mass balance equation applied to the adsorption column:

$$q_e = \frac{1}{m}\int_0^{t_s} \left(F_{CO_{2,in}} - F_{CO_{2,out}}\right) dt \quad (1)$$

where m is the mass of the sorbent in the bed, $FCO_{2,in}$ and $FCO_{2,out}$ represent the molar flow rates of CO_2 at the inlet and outlet of the bed, respectively, t_s is to the time required to saturate the sorbent bed.

ii) t_b – The breakthrough time is defined as the time at which the CO_2 concentration at the outlet of the column reached 5 % of the inlet concentration. This marks the point when the reactor is taken offline for regeneration. A longer t_b indicates a higher effective capture capacity of the sorbent.

iii)$\Delta\tau = t_{70} - t_{10}$ – The time parameter, where t_{70} and t_{10} represent the times at which the CO_2 concentration at the outlet reaches 10 % and 70 % of the inlet concentration, respectively, is closely related to the slope of the linear portion of the breakthrough curve. A smaller $\Delta\tau$ indicates a steeper breakthrough curve, reflecting a faster adsorption

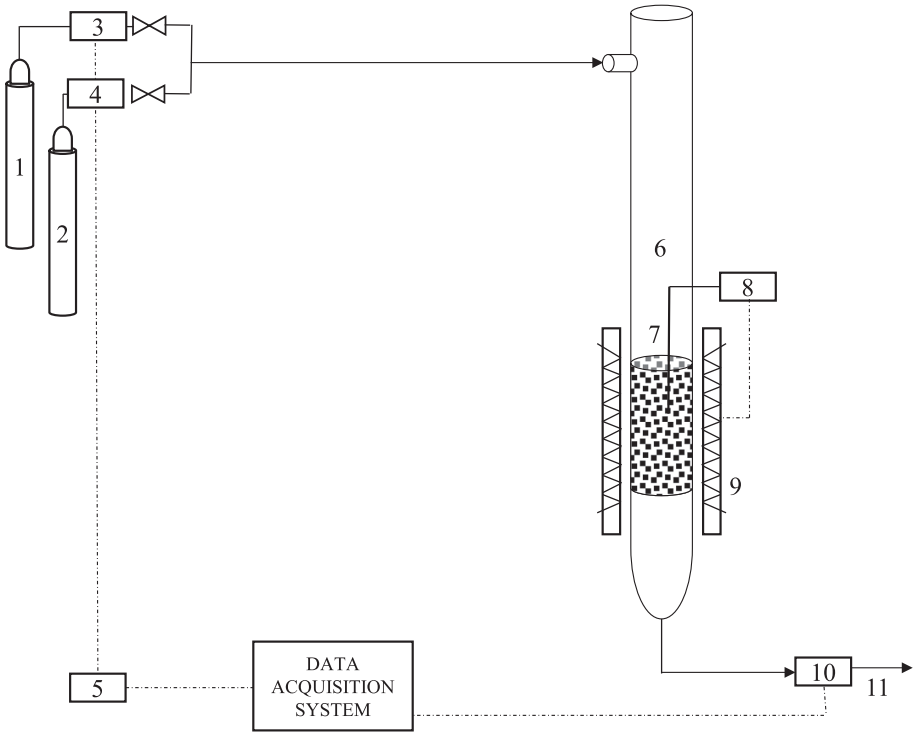


Fig. 1. Experimental apparatus: 1) N_2 cylinder; 2) CO_2 cylinder; 3) N_2 mass flow controller; 4) CO_2 mas flow controller; 5) multichannel control instrument; 6) 6 mm ID fixed bed reactor; 7) thermocouple; 8) temperature controller; 9) heating jacket; 10) CO_2 analyzer; 11) stack.

process.

iv)ψ − The fraction of bed used at the breakpoint represents the percentage of CO_2 adsorbed up to the breakthrough time, t_b, relative to the total amount adsorbed at full saturation. This parameter indicates that bed utilization efficiency before regeneration is required.

2.2.1.1. Adsorption thermodynamics. The adsorption equilibrium is generally characterized by adsorption isotherms, which graphically depict the relationship between the equilibrium CO_2 uptake and the CO_2 partial pressure at equilibrium, all measured at a constant temperature. The equilibrium CO_2 uptake at specific temperatures and partial pressures was determined by integrating breakthrough curves [25]. The Sips isotherm model [39] was used to describe the experimental adsorption isotherms of the CALF-20. Detailed information on the Sips isotherm is reported in the Supporting Information. In summary, this model, designed for heterogeneous systems, combines the features of both the Langmuir and Freundlich isotherms, offering a more versatile approach for capturing the adsorption behavior. The general form of the Sips isotherm equation is:

$$q_e = q_m \frac{K_S (P_{CO_2})^{1/n}}{1 + K_S (P_{CO_2})^{1/n}} \quad (2)$$

Where, q_e (mmol g^{-1}) is the amount of CO_2 adsorbed per unit mass of the sorbent, q_m (mmol g^{-1}) is the maximum adsorption capacity, P_{CO_2} (atm) is the partial pressure of CO_2 at equilibrium, K_S ($atm^{-1/n}$) is the Sips constant (related to the affinity of the adsorbent for the adsorbate), n is the dimensionless heterogeneity factor, indicating the degree of heterogeneity of the adsorbent surface ($1/n > 1$ suggests a heterogeneous surface; the higher this parameter, the greater is the heterogeneity of the system). Instead of relying on linearization techniques, which can introduce complications when dealing with nonlinear isotherm equations, a nonlinear regression analysis was applied to ensure a more accurate fit [40].

The accuracy of the Sips model in fitting the experimental isotherm data was evaluated by calculating the correlation coefficient (R^2), which ranges from 0 to 1, and the HYBRID error function, specifically designed to improve the fit of the sum of squared errors (SSE) method at low partial pressures [41](lower HYBRID values indicate a higher quality fit). The HYBRID error function is defined as follows:

$$HYBRID(\%) = \frac{100}{n-p} \sum_{i=1}^{i=n} \left[\frac{\left(q_{mod_i} - q_{exp_i}\right)^2}{q_{exp_i}} \right] \quad (3)$$

in which q_{exp} and q_{mod} represent the experimental and modeled adsorption uptakes, respectively; n and p are the total count of experimental data points and parameters in the isotherm equation (which is 3 in the case of the Sips model), respectively.

The isosteric heat of adsorption Q_{st} [42] is a key parameter in adsorption studies, representing the heat released during adsorption at a constant adsorbate amount. It can be calculated from the Clausius-Clapeyron equation by plotting $\ln(P_{CO2})$ versus 1/T at fixed coverage [14,25,43,44] (see the Supporting Information for more detailed information). In summary, it reveals the strength of molecular interactions between the adsorbate and adsorbent surface, with higher Q_{st} values indicating stronger interactions and, therefore, greater adsorbent affinity for CO_2. Generally, $Q_{st} < 80$ kJ mol^{-1} denotes physisorption, while Q_{st} between 90–100 kJ mol^{-1} suggests strong chemisorption [35,40,43]. Additionally, the magnitude and variation of Q_{st} with surface coverage provide insight into surface heterogeneity; a constant Q_{st} implies a homogeneous surface, while changes indicate heterogeneity [35,40,43].

2.2.1.2. Adsorption kinetics. Predicting the kinetic parameters of the adsorption process is often complex; therefore, the most common approach involves fitting experimental data to various apparent kinetic models and selecting the one that provides the best fit [45–48]. These apparent models consolidate all adsorption steps, including mass transfer resistances like external diffusion, pore diffusion, and surface adhesion, into a unified framework [45–48].

The pseudo-first-order [49] and pseudo-second-order [50] models are among the simplest and most commonly applied kinetic models available [45–48]. Here the term "pseudo" simply indicates that the rate laws are expressed in terms of the adsorbed amount (q, representing occupied adsorption sites), instead of the concentration of the species being adsorbed [51–54]. Detailed information on both these kinetic models is reported in the Supporting Information.

The pseudo-first-order kinetic model, proposed by Lagergren in 1898 [49], assumes that the adsorption rate is proportional to the number of unoccupied active sites, making it ideal for describing reversible interactions, such as CO_2 adsorption onto physisorbents like zeolites, activated carbons, and MOFs [49,55]. In contrast, the pseudo-second-order model, introduced by Blanchard et al. [50], assumes the adsorption rate is proportional to the square of available sites, accounting for both physical and chemical interactions, and is thus better suited for chemisorption [50]. Their integrated mathematical equations are:

First-order

$$q_t = q_e \left[1 - exp\left(-k_f t\right)\right] \quad (4)$$

Second-order

$$q_t = \frac{q_e^2 k_s t}{1 + q_e k_s t} \quad (5)$$

where q_t (mmol g^{-1}) represents the extent of CO_2 adsorbed at time t, and k_f (min^{-1}) and k_s (g $mmol^{-1}$ min^{-1}) are the rate constants for first-order and second-order adsorption model, respectively.

The accuracy of the kinetic models in fitting the experimental data was determined by calculating the regression coefficient (R^2) and hybrid fractional error function (HYBRID), as defined in Eq. (3). After calculating the kinetic constant, the activation energy (E_a), which represents the minimum energy required for the adsorbate molecules to overcome [56], was determined using the Arrhenius equation [25].

2.2.2. Desorption

Temperature swing adsorption (TSA) methodology was employed to perform CO_2 desorption experiments. Each desorption test was preceded by an adsorption phase at 28 °C with a 15 %vol. CO_2 concentration, following the protocol outlined in relative experimental section. The CO_2 desorption process, which simultaneously regenerated the sorbent, involved an isothermal N_2 purge. Specifically, subsequent to bed saturation, the apparatus was heated to the target desorption temperature (40, 70, 100, 130, or 150 °C), and N_2 was introduced through the heated sorbent bed at a flow rate of 15 L/h. This methodology facilitated CO_2 recovery through the combined effects of increased temperature and reduced CO_2 partial pressure.

For each CO_2 desorption test, CO_2 desorption profiles, i.e. C versus time, were obtained and the key desorption parameters were determined:

v) The extent of desorption, q_{des}, was calculated using the same procedure as that used for the evaluation of the amount of CO_2 adsorbed, according to Eq. (1).

vi) The CO_2 recovery level, R, was defined as the proportion of adsorbed CO_2 that is released/recovered during the desorption process. This was expressed as a percentage of the total amount of CO_2 initially adsorbed:

$$R = \frac{q_{des}}{q_e} \bullet 100 \quad (6)$$

vii) The desorption time, t_d, was defined as the duration of the CO_2 desorption process. It was measured from the start of the N_2 purge at the specified desorption temperature until the desorption step ended (i.e. when R = 100 %). Multiple partial desorption times, t_i, were

additionally evaluated, each corresponding to a different CO_2 recovery level (R < 100 %)., i.e. prior to the full conclusion of the desorption step.

viii) The mean CO_2 concentration in the desorbing stream, C_m, was evaluated as the average concentration of CO_2 in the outlet stream during the desorption process at different desorption times and different levels of recovery.

The cyclic stability of CALF-20 was also assessed performing ten adsorption/desorption cycles (Adsorption: C_0 = 15 %vol., T = 28 °C; Desorption: C_0 = 0 %vol., T = 150 °C).

3. Results and discussion

3.1. Materials characterization

The XRD patterns of the milled powders together with the calculated reference spectra are shown in Fig. 2. After 30 min of milling, the initial reagents have disappeared, and the CALF-20 phase is well defined. The broad peaks suggest a crystallite size of nanometric dimensions. By extending the synthesis duration, the CALF-20 phase increases its crystallinity without the appearance of peaks attributable to secondary phases. Crystallite size increases from 65 ± 2 nm to 171 ± 4 nm, suggesting an improvement in the crystal quality without any change in the powder composition.

SEM analysis confirms the X-ray evidence. Particles morphology and size are affected by reaction time as shown in Fig. 3a-d. SEM observation of the CALF20BM05H sample shows agglomeration of crystals with a fairly narrow size distribution and dimensions of approximately

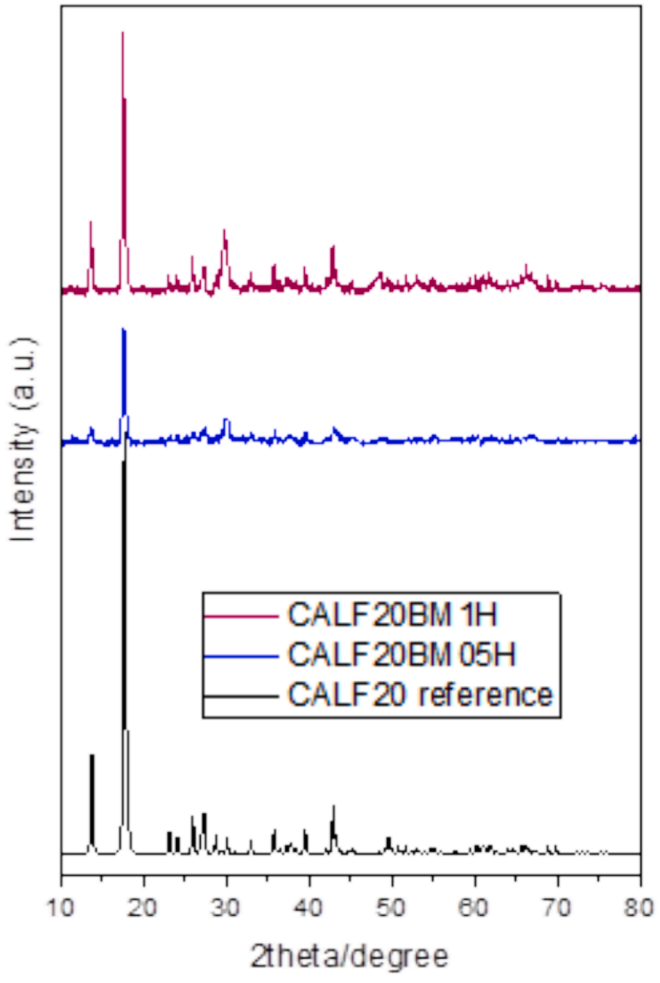


Fig. 2. XRD patterns of powders obtained after 30 min of milling (CALF20BM05H) and 1 h (CALF20BM1H).

100–200 nm, which is larger than the crystallite size evaluated by XRD. This finding suggests that the crystalline nature of the material is rather poor. The sample was found uniform. The increase in milling time clearly induces the growth of larger crystals (Fig. 3c and d) as already hypothesized from the observation of the diffraction spectra. Further extending the milling time to two hours (data not shown) resulted in a material with a comparable surface area and crystal quality. Consequently, it was not considered for additional adsorption studies, as the sustainability of the synthesis was prioritized. Moreover, it is well known that excessive milling durations can lead to the formation of aggregates and agglomerates, with limited adsorptive properties [57].

Textural properties were determined from N_2 adsorption/desorption isotherms at 77 K, as shown in Fig. 4 for the sample CALF20BM1H. The curve is typical of a microporous material (type 1), with a rapid uptake at low partial pressures. Soon after the knee, the slope at intermediate pressure regime suggests a non-negligible extension of "non-microporous" surface, in accordance with the presence of a slight hysteresis, indicating a limited mesoporous volume. The BET specific surface was determined using the Rouquerol criteria [34] and does not show the expected increase based on the improved crystallinity observed by XRD measurement. The measured specific surfaces settle on very similar values, i.e. 338 ± 10m^2g^{-1} for CALF20BM05H and 350 ± 15 m^2g^{-1} for CALF20BM1H. Such values are indicative of a structural disorder that is typical of materials synthesized by mechanochemistry. Post-synthetic treatments such as aging in solvent generally significantly improve the crystallinity of the materials and their specific surface to the detriment of the advantages of a rapid and solvent-free mechanochemical synthesis. Therefore, the gas adsorption and desorption properties aimed at TSA studies were carried out on the as-synthesized materials.

3.2. Adsorption

Fig. 5a and b present the breakthrough curves, with Fig. 5a showing data for different CO_2 inlet concentrations at 28 °C, and Fig. 5b displaying curves for a 15 % CO_2 inlet concentration across various adsorption temperatures. Comparable patterns were observed across all the examined input CO_2 levels and temperature conditions. The adsorption isotherms and relevant adsorption parameters are provided in Figs. 6 and 7, respectively.

The analysis of these data highlights that the effects of temperature and pressure on CO_2 adsorption vary depending on whether the process is viewed from a thermodynamic or kinetic perspective. The CO_2 adsorption capacity, q_e, representing the amount of CO_2 adsorbed at thermodynamic equilibrium, increases as P_{CO2} rises (Fig. 6, in which markers indicate the experimental data points), aligning with the fact that P_{CO2} serves as the driving force for adsorption from a thermodynamic perspective.

Conversely, q_e decreases with increasing temperature, indicating that the adsorption isotherms become less favorable, which is consistent with the adsorption process being exothermic. As the temperature rises, more energy is transferred to the CO_2 molecules in the gas phase, accelerating their diffusion. However, at higher temperatures, the more energized CO_2 molecules are less likely to be captured on the sorbent surface. In fact, as the temperature increases, the adsorbed CO_2 can more easily desorb and return to the gas phase, as the molecules gain sufficient energy to overcome the attractive forces from the adsorbent surface. Additionally, CO_2 molecules in the gas phase are more inclined to remain there rather than adsorb onto the surface [58].

From a kinetic perspective, both temperature and P_{CO2} positively influence the CO_2 adsorption rate, making the process faster and reducing the time required to reach equilibrium. This is evident from the decrease in $\Delta\tau$ and the increase in ψ as either temperature or PCO_2 increases. The steepening of the breakthrough curves with rising temperature or P_{CO2} further illustrates this effect (Fig. 5). Regarding the adsorption temperature, the faster mass transfer at higher temperatures is due to the increased mobility of CO_2 molecules [59]. Similarly,

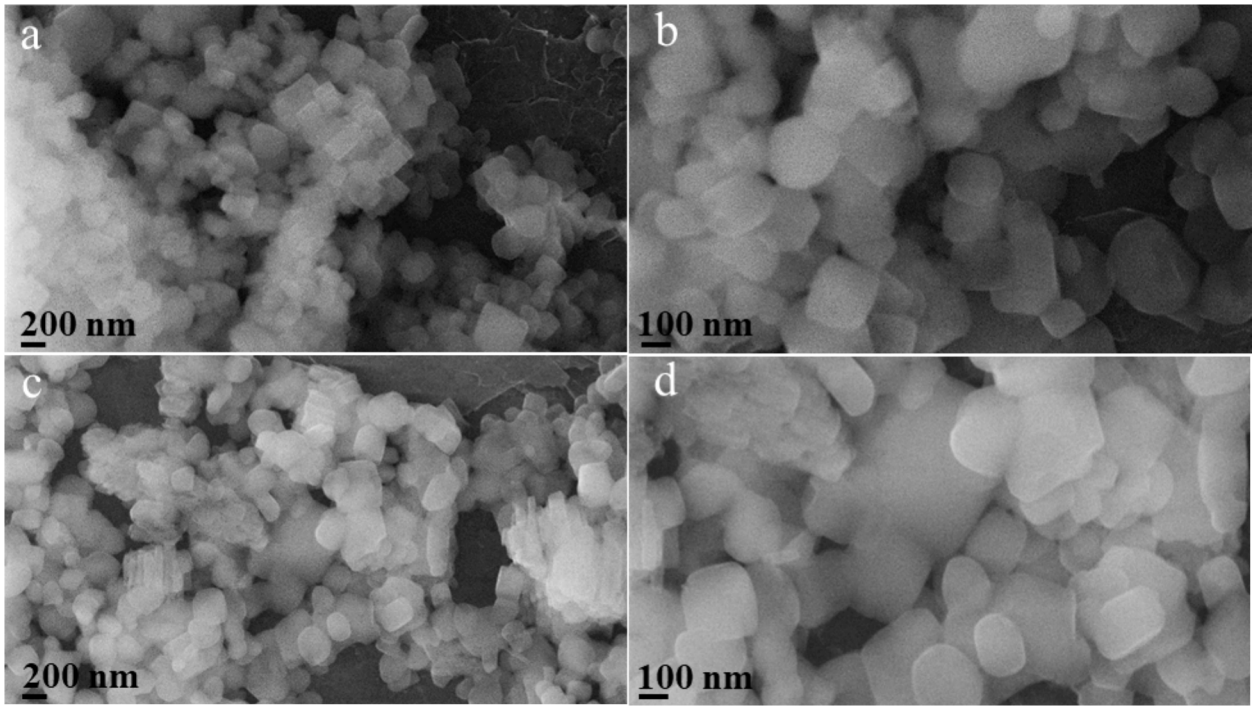


Fig. 3. SEM images at two different magnifications of CALF20BM05H (a-b) and CALF20BM1H (c-d) obtained after 30 min and 1 h milling respectively.

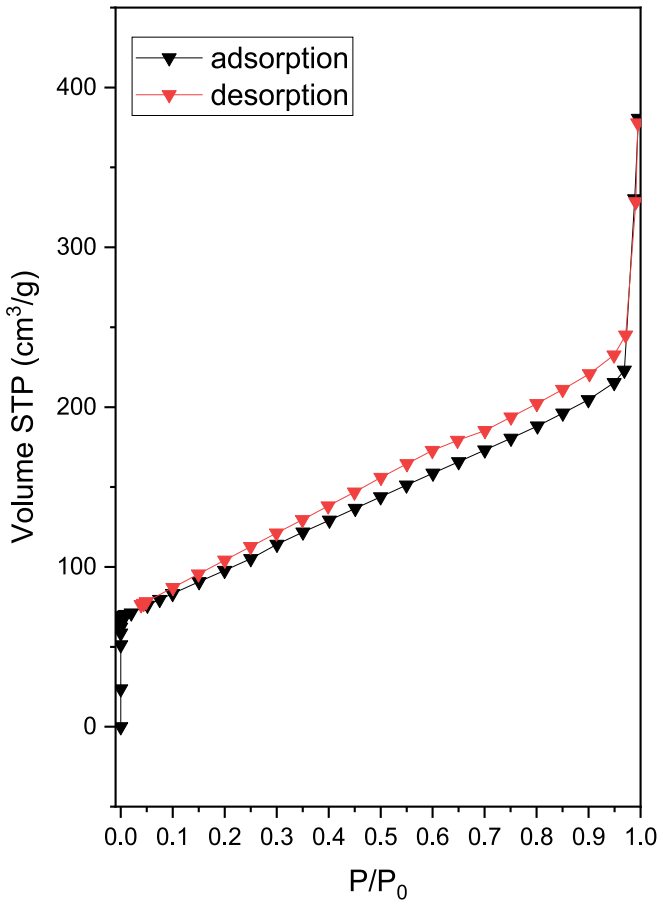


Fig. 4. Nitrogen adsorption/desorption isotherm at 77 K on CALF20BM1H.

increasing P_{CO2} speeds up the adsorption process, primarily because the higher partial pressure enhances the mass transfer rate by providing a stronger adsorption driving force [59]. In contrast, lower CO_2 partial pressures lead to slower breakthrough curves, as the CO_2 concentration front takes longer to reach the bed outlet [9,26,47]. This behavior aligns with the findings of numerous studies on CO_2 adsorption using physical sorbents [9,26,47]. In contrast, both temperature and P_{CO2} have a negative impact on the breakthrough time t_b, which decreases as either parameter increases. The reduction in t_b with higher temperatures is due to the combined effects of lower adsorption capacity and a faster adsorption rate, both of which contribute to quicker bed saturation. The influence of P_{CO2} requires a more nuanced explanation, as it involves the interaction of two opposing factors. On one hand, from a thermodynamic perspective, higher P_{CO2} enhances the adsorption capacity of the sorbent, which would normally increase t_b. On the other hand, the higher P_{CO2} accelerates the adsorption process, leading to faster saturation of the bed and thus a decrease in t_b. Ultimately, the latter effect dominates, causing t_b to shorten despite the increased adsorption capacity.

To better evaluate the performance of CALF-20, a comparison was conducted against benchmark materials reported in the literature under comparable conditions, as summarized in Table 1. CALF-20, synthesized in this work via mechanochemical method, exhibits a CO_2 adsorption capacity of 2.55 mmol g^{-1} at a temperature of 301 K and a PCO_2 of 0.2 atm. This value is slightly higher than the capacity reported by Lin et al. [21] (2.10 mmol g^{-1} at T = 303 K and PCO_2 = 0.2 atm) for CALF-20 synthesized via solvothermal method under the same operating conditions.

The adsorption capacity of CALF-20 also compares favorably with other MOFs widely studied for CO_2 capture. For instance, CALF-20 outperforms HKUST-1 (1.14 mmol g^{-1} at 298 K and 0.15 atm) and ZIF-8 (0.12 mmol g^{-1} at 298 K and 0.1 atm) under low-pressure conditions, despite having a smaller surface area (350 m^2 g^{-1} for CALF-20 versus 680 m^2 g^{-1} for HKUST-1 and 1135 m^2 g^{-1} for ZIF-8). This highlights the efficient utilization of CALF-20 pore structure for CO_2 adsorption.

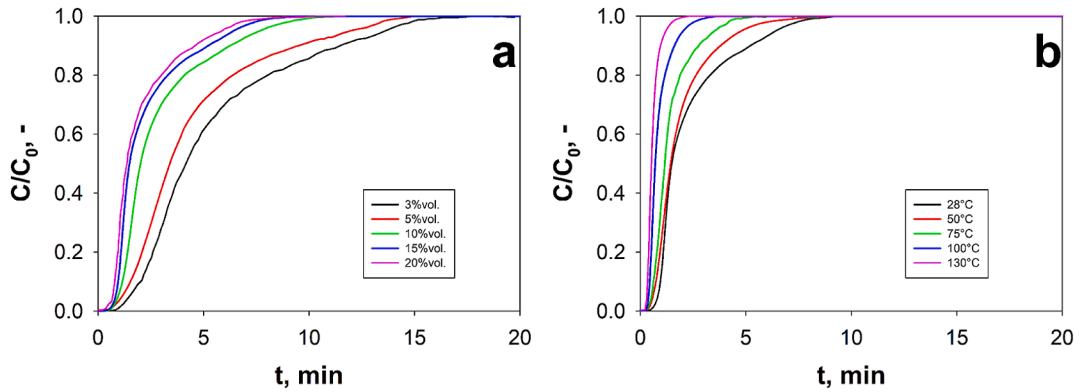


Fig. 5. CO_2 adsorption breakthrough curves on CALF-20: a) at a constant adsorption temperature of 25 °C and varying the inlet CO_2 concentrations; b) at a fixed inlet CO_2 concentration of 15 %vol. and changing the adsorption temperature.

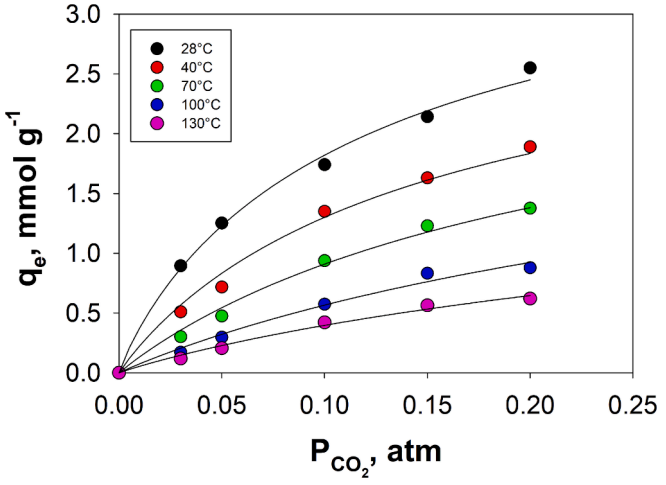


Fig. 6. CO_2 adsorption isotherms obtained for CALF-20 and fitted by the Sips model.

3.2.1. *Adsorption thermodynamics*

Fig. 6 presents the fitting of the experimental isotherm curves using the Sips equation. The experimental data points are indicated by markers, while the solid lines represent the predictions from the isotherm models. The Sips model parameters, along with the R^2 values and HYBRID error function results, are detailed in Table 2. Fig. 6 clearly demonstrates that the Sips model aligns well with experimental data, consistent with findings from other studies using physisorbents [64–68]. This is further supported by the high R^2 values, which consistently exceed 0.99, and the HYBRID error values, which remain below 1.5 %. These results suggest that the adsorption process involves a heterogeneous surface with a range of adsorption site affinities. Indeed, the Sips model is well-suited for capturing this complexity, as it combines the flexibility of the Freundlich isotherm at low pressures, which accounts for non-uniform adsorption energies, with the Langmuir isotherm at high pressures, where adsorption saturation occurs. This hybrid approach makes the Sips model particularly effective in describing the adsorption behavior of materials with varied surface characteristics, such as CALF-20. In fact, the results from the Sips model reveal that the values of n are greater than 1, thus confirming a degree of energetic heterogeneity on the solid surface and also suggesting a strong adsorption intensity [39,69,70].

Table 2 also shows that increasing the temperature leads to a reduction in both the predicted maximum CO_2 adsorption capacity (q_m) and the adsorption isotherm constant (K_S). This trend is consistent with the exothermic nature of CO_2 adsorption on CALF-20, meaning that the process is more thermodynamically favorable at lower temperatures.

Fig. 8a presents the adsorption isosteres for CALF-20, which illustrates the relationship between $\ln(P_{CO2})$ and the inverse of absolute temperature at constant loading (0.005 – 0.550 mmol g^{-1}) across the investigated temperature range of 28 – 130 °C. The Clausius–Clapeyron equation was then applied to evaluate the isosteric heat of adsorption, Q_{st}. Specifically, it was derived from the slopes (Q_{st} /R) of these isosteres, and plotted as a function of the surface loading (Fig. 8b).

The negative slopes observed in all isosteres confirm the exothermic nature of CO_2 adsorption. The magnitude and variation of Q_{st} during CO_2 adsorption, particularly as surface loading increases, offer critical details about the molecular-scale bonding dynamics occurring between CO_2 and the adsorbent, while also revealing the energetic heterogeneity of the solid surface [40]. Notably, CALF-20 exhibits Q_{st} values within the range 22–29 kJ mol^{-1}, suggesting physical adsorption (< 80 kJ mol^{-1}) [58]. This indicates that the adsorption process is predominantly driven by physical forces such as Van der Waals interactions, hydrophobicity, and other physisorption mechanisms [71]. This result aligns with existing literature, which highlights that MOFs are predominantly physisorbent materials, characterized by relatively low Qst values due to the physical nature of the adsorption interactions. These values generally fall within the range 10–50 kJ mol^{-1}, depending on the specific MOF structure, and are significantly lower than those associated with chemisorption processes (>80 kJ mol^{-1}). This inherent property of MOFs makes them particularly well-suited for applications requiring reversible adsorption and energy-efficient regeneration, such as TSA processes. However, within the domain of MOF physisorbents, it is possible to identify distinct ranges of Q_{st} values that correspond to varying strengths of interaction, which can influence the material performance:

- Low-Q_{st} MOFs (< 20 kJ mol^{-1}) – Examples include IRMOF-1 (10 kJ mol^{-1}), MOF-177 (12 kJ mol^{-1}), MIL-53 (12.5 kJ mol^{-1}), ZIF-8 (15.5 kJ mol^{-1}) and UiO-66(Zr) (16.1 kJ mol^{-1}) [72]. These MOFs exhibit very weak interactions with the adsorbate, leading to very low regeneration energy requirements. Such MOFs prioritize minimal energy costs but are generally less selective for specific gases such as CO_2. They are better suited for applications where capacity and selectivity are less critical than operational efficiency.
- Moderate-Q_{st} MOFs (20–35 kJ mol^{-1}) – This category includes, besides the CALF-20 presented in this work, HKUST-1 (25.4 kJ mol^{-1}), MIL-101(Cr) (32 kJ mol^{-1}), MFM-102 (24 kJ mol^{-1}) and MOF-808 (34 kJ mol^{-1}) [30], which demonstrate slightly stronger interactions. These MOFs are particularly advantageous in TSA processes where energy efficiency and operational stability are critical.
- High-Q_{st} MOFs (35–45 kJ mol^{-1}) – MOFs like Mg-MOF-74 (38.9 kJ mol^{-1}) and NKU-521 (41 kJ mol^{-1}) fall within this range [30,72]. These materials demonstrate stronger interactions with CO_2,

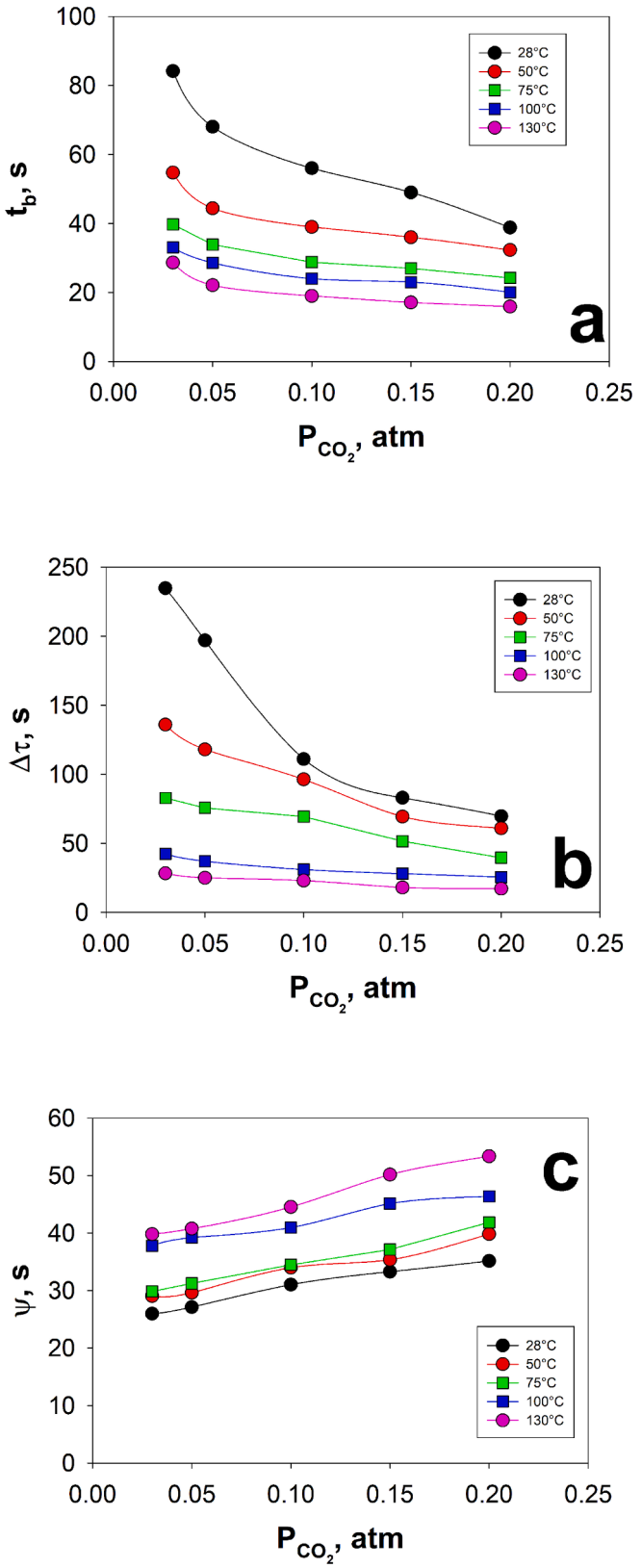


Fig. 7. Adsorption parameters: a) Breakthrough time (t_b); b) time parameter ($\Delta\tau$); c) fraction of bed utilized at t_b (ψ), as functions of the CO_2 partial pressure (P_{CO2}) for all the investigated temperatures.

Table 1
Comparison of CO_2 adsorption performances of different types of MOFs with corresponding process conditions.

Sorbent	Surface area $m^2\ g^{-1}$	T K	P_{CO2} atm	Ads. capacity mmol/g	Ref.
CALF-20	*350*	*301*	*0.10/0.15/0.20*	*1.74/2.14/2.55*	*This work*
		323		*1.35/1.63/1.89*	
CALF-20	528	303	0.10/0.15/0.2	1.79/1.98/2.10	[21]
		323		1.14/1.41/1.64	
HKUST-1	680	298	0.15	1.14	[60]
HKUST-1	1800	298	0.10/1.00	0.93/5.72	[32]
MOF-508	323	323	0.10	0.10	[61]
Fe3O4@HKUST-1	830	298	0.10/1.00	0.45/3.51	[32]
HKUST-1	–	295	0.10	0.62	[62]
IRMOF-1	1892	298	0.10	0.08	[62]
ZIF-8	1135	298	0.10	0.12	[62]
MIL-47	600	298	0.10	0.18	[62]
UMCM-1	4034	298	0.10	0.09	[62]
MOF-2	345	298	1.00	0.80	[63]
IRMOF-11	2096	298	1.00	1.91	[63]
MOF-74	816	298	1.00	4.45	[63]
$Cu_3(BTC)_2$	1781	298	1.00	4.08	[63]
MOF-505	1547	298	1.00	3.42	[63]

Table 2
Sips isotherm model and fitting quality parameters.

T °C	K_S atm^{-1}	q_m mmol/g	1/n –	R^2 –	Hybrid %
28	6.488	4.065	1.107	0.998	0.482
50	5.910	3.270	1.051	0.996	1.436
75	4.053	3.009	1.030	0.996	1.183
100	2.464	2.706	1.032	0.992	0.871
130	2.139	2.021	1.061	0.993	0.674

resulting in higher selectivity but at the cost of increased energy requirements during regeneration.

The synthesized CALF-20, with Qst values of 22–29 kJ mol^{-1}, is positioned at the moderate end of the spectrum. Its performance aligns with the need for energy-efficient regeneration in TSA processes, offering a balance between selectivity and energy cost. Additionally, the moderate Q_{st} values contribute to enhanced cyclic stability, as the relatively low energy required for desorption reduces thermal and mechanical stress on the material during repeated adsorption/desorption cycles. This ensures that CALF-20 maintains its structural integrity and adsorption performance over extended operational periods, making it particularly well-suited for industrial applications requiring consistent and reliable performance under high-frequency cycling conditions.

With reference to the dependence of Q_{st} on the surface loading, a clear decline in Q_{st} can be observed as the CO_2 surface loading increases. The molecular-level interactions responsible for this trend can be attributed to a combination of three key factors [73]: (1) the heterogeneity of the adsorbent surface, (2) the nature of adsorbate-adsorbent interactions, (3) the role of adsorbate–adsorbate interactions [74]. Specifically, these contributions are as follows:

- Surface heterogeneity – The variation in adsorption site affinities on CALF-20, as indicated by Sips isotherm parameters, contributes to the observed decline [73,75].
- Adsorbate-adsorbent interactions – At low coverage, CO_2 molecules bind to the most energetically favorable sites (i.e. the strongest binding sites), often associated with coordinatively unsaturated

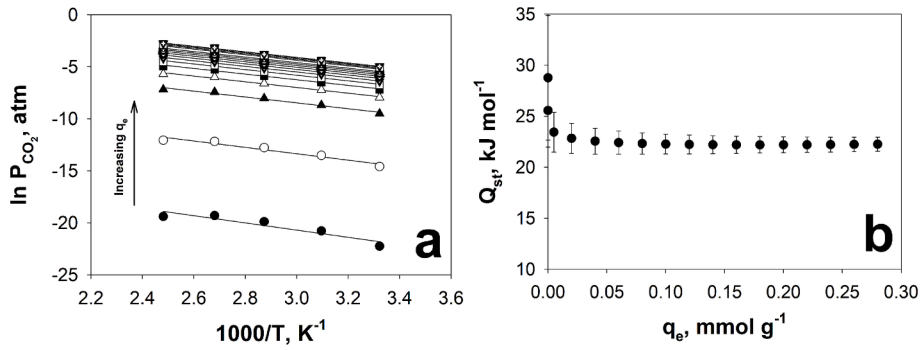


Fig. 8. A) adsorption isosteres of co$_2$ on the CALF-20; temperature range: 28–130 °C; CO_2 loading (q_e) ranging from 5 10^{-7} to 0.30 mmol/g. b) Q_{st} as a function of the CO_2 loading.

metal centers or functional groups, resulting in high Q_{st} [73,75,76]. As adsorption progresses, these high-energy sites become occupied, forcing CO_2 to adsorb onto weaker sites, reducing Q_{st} [73].

- Adsorbate-adsorbate interactions – At higher loadings, interactions between adsorbed CO_2 molecules, including repulsive quadrupole forces and weaker London dispersion forces [74,77,78], further raises the activation energy, leading to a continued decline in Q_{st} [79,80]

3.2.2. *Adsorption kinetics*

The transient CO_2 adsorption uptakes on CALF-20, derived from the experimental breakthrough curves at 15 % CO_2 inlet concentration, are shown in Fig. 9a for various adsorption temperatures. To emphasize the impact of temperature more clearly, these uptake curves are also presented as dimensionless fractional uptake (q_t/q_e) in Fig. 9b.

The data in Fig. 9 confirms that temperature has contrasting effects on adsorption kinetics and thermodynamics. As the temperature rises, CO_2 adsorption occurs more rapidly due to improved kinetic processes, but the equilibrium amount of CO_2 adsorbed decreases because of thermodynamic limitations. Specifically, as the temperature increases the equilibrium CO_2 adsorption capacity declines, as shown in Fig. 9a by the decreasing asymptotic values in the uptake curves, which is consistent with the exothermic nature of the process. Conversely, higher temperatures enhance adsorption kinetics, as evidenced by the steeper curves in Fig. 9b, reflecting the reduced time required to reach equilibrium. This acceleration is attributed to faster mass-transfer and diffusion processes at elevated temperatures.

Then both the pseudo-first-order and pseudo-second-order kinetic models were used to fit the experimental data. The experimental data are compared with the theoretical predictions in Fig. 10, where the data points correspond to the experimental values and the dashed lines represent the model predictions. The kinetic constants, along with the corresponding correlation coefficients and error values, are summarized in Table 3.

The fitting quality provided by the pseudo-first-order kinetic model is consistently more accurate than that of the pseudo-second-order model across all temperatures. In comparison, the pseudo-second-order model shows larger discrepancies, particularly underestimating CO_2 uptake during the initial minutes ($t < 10$ min) and overestimating it as equilibrium is approached. This leads to a significant overestimation of the equilibrium CO_2 adsorption capacity (q_e), as shown in Table 3. On the contrary, the pseudo-first-order model provides a more reliable fit throughout the entire adsorption process, capturing the time evolution of the data more effectively. This improved fit is further confirmed by higher R^2 values and lower HYB (%) values, as reported in Table 3. Additionally, it is also noteworthy that, increasing the temperature, the kinetic constants of both the models (k_f and k_s) show a clear increase (Table 3).

The reasons for these results, namely the good fit of the pseudo-first-order kinetic model and the poor fit of the pseudo-second-order model are as follows:

- Physical nature of adsorption – As previously discussed, the adsorption of CO_2 on CALF-20 is dominated by physisorption, as supported by Q_{st} values (22–29 kJ/mol), i.e. indicating that the process is governed by weak van der Waals forces rather than strong chemical bonds. The pseudo-first-order kinetic model assumes that the adsorption rate is directly proportional to the number of unoccupied active sites [49], a behavior that aligns well with the weak, reversible interactions of the observed physisorption-dominated process [81]. In contrast, the pseudo-second-order model assumes that the adsorption rate depends on the square of the unoccupied site concentration [50], a behavior more characteristic of chemisorption, where stronger interactions and covalent bonding are involved [81]. This fundamental discrepancy leads the pseudo-second-order model to overestimate the influence of chemisorptive interactions, resulting in poor alignment with the experimental data.

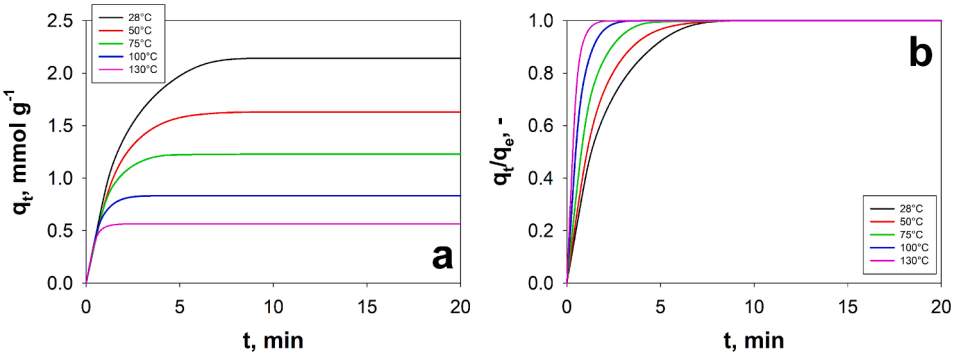


Fig. 9. Transient CO_2 adsorption uptake on CALF-20 in dimensional (a) and dimensionless (b) form at all the investigated temperatures. C_0 = 15 %vol.

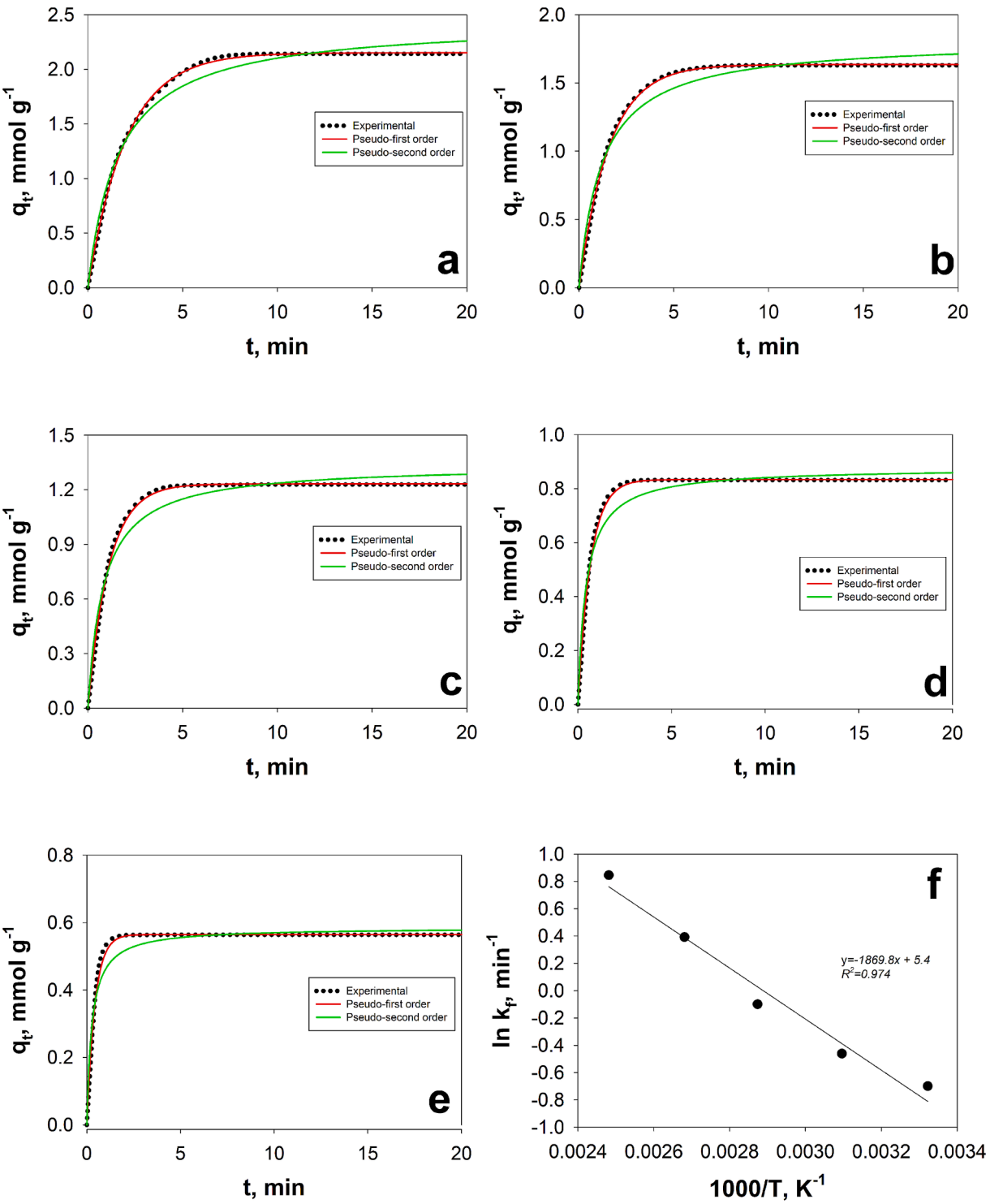


Fig. 10. Experimental and modelled transient CO_2 uptake on CALF-20 at: a) 28 °C; b) 50 °C; c) 75 °C; d) 100 °C; e) 130 °C. f) Arrhenius plot. C_0 = 15 %vol.

- Initial and equilibrium predictions – The pseudo-second-order model fails to accurately capture the adsorption dynamics during both the initial and equilibrium stages of the process. At the early stages of adsorption (t < 10 min), the pseudo-second-order model underestimates the rapid CO_2 uptake observed experimentally, reflecting its inability to account for the strong influence of diffusion and surface interactions that dominate during this phase [81]. Near equilibrium, the model overestimates the adsorption capacity, likely due to its assumption of stronger interactions than those present in the system. Conversely, the pseudo-first-order model effectively fits the entire process, accurately representing both the rapid initial uptake and the equilibrium behavior.
- Temperature effects – Our experiments reveal that temperature plays a significant role in the adsorption kinetics. Higher temperatures enhance molecular diffusion and mass transfer rates (i.e. CO_2 molecules move faster, enhancing their ability to reach and interact with the active sites on CALF-20), leading to faster adsorption. In physisorption, weak van der Waals interactions remain largely reversible even at elevated temperatures. The pseudo-first-order model captures this proportional relationship between adsorption rate and

Table 3
Parameters and fitting quality of the pseudo-first order and pseudo-second order kinetic models. C_0 = 15 %vol.

Kinetic model	T °C	q_e mmol/g	k_f/k_s min^{-1}	R^2 –	Hybrid %
First-order	28	2.152	0.497	0.99997	0.023
	50	1.635	0.630	0.99999	0.021
	75	1.232	0.905	0.99997	0.005
	100	0.834	1.480	0.99989	0.014
	130	0.565	2.329	0.99963	0.014
Second-order	28	2.442	0.254	0.870	0.493
	50	1.816	0.455	0.870	0.452
	75	1.338	0.909	0.870	0.112
	100	0.878	2.591	0.869	0.212
	130	0.585	6.389	0.867	0.131

active site availability, adapting well to temperature-driven changes [81]. The pseudo-second-order model, on the contrary, assumes stronger and more complex chemisorption-like interactions, making it less sensitive to temperature-driven diffusion effects and failing to accurately predict the experimentally observed increase in adsorption rate [81].

- Pressure effects – CO_2 partial pressure also strongly impacts adsorption kinetics. Higher pressures increase CO_2 concentration in the gas phase, boosting collision frequency and strengthening the driving force for adsorption. In physisorption-dominated systems, the adsorption rate rises proportionally with pressure as more molecules temporarily bind to the surface. The pseudo-first-order model reflects this linear relationship between active sites and adsorption rate, matching experimental observations. Conversely, the pseudo-second-order model, which assumes adsorption rate depends on the square of unoccupied site concentration, overemphasizes site interactions and fails to represent the simple pressure-driven behavior observed in physisorption [81].

Given that the pseudo-first-order kinetic model provides the best representation of the adsorption process, the corresponding kinetic coefficients at different temperatures were used to calculate the activation energy and pre-exponential factor by applying linear regression to the linearized form of the Arrhenius equation [25]. The linearized Arrhenius plots are shown in Fig. 10f. The positive value of E_a confirms that an increase in temperature leads to a higher reaction rate. Specifically, the activation energy obtained (15.5 kJ mol^{-1}) is consistent with data reported in other studies on physisorbents [82–84]. This relatively low value further supports the conclusion that the CO_2 adsorption on CALF-20 involves weak physical interactions.

3.3. Desorption

The CO_2 desorption profiles, obtained at different desorption temperatures, are displayed in Fig. 11. The desorption process exhibits a characteristic pattern consisting of an initial peak followed by a prolonged tail. At all examined temperatures, the CO_2 outlet concentration reaches its maximum value rapidly, within 1.5 min, suggesting that the majority of adsorbed CO_2 is swiftly released from the samples. Subsequently, the curves display a more gradual, extended tail, indicating that the remaining CO_2 desorbs at a slower rate due to a decrease in the driving force. Regardless of the desorption temperature, the desorption process is completed within 3 min.

It is also important to point out that CALF-20 demonstrates complete regeneration capability, with the quantity of CO_2 desorbed matching the amount adsorbed in the preceding adsorption phase across all tested temperatures. Furthermore, the experimental data demonstrate that the desorption process is remarkably affected by the desorption temperature. Indeed, the desorption rate increases with rising temperature, as evidenced by the desorption profiles becoming narrower and taller at higher temperatures, indicating a faster process. On the contrary, as temperature decreases, the desorption curve shifts to the right, showing slower desorption with a broader peak. This behavior reflects the temperature-dependent kinetics of CO_2 desorption, with higher temperatures enhancing the rate of CO_2 release. The desorption time, i.e. the time required to release the previously adsorbed CO_2, decreases as the desorption temperature increases, making higher temperatures an effective way to shorten regeneration time. This improvement in desorption rate can be ascribed to two factors: the reduced CO_2 adsorption capacity (promoting desorption) and the increased

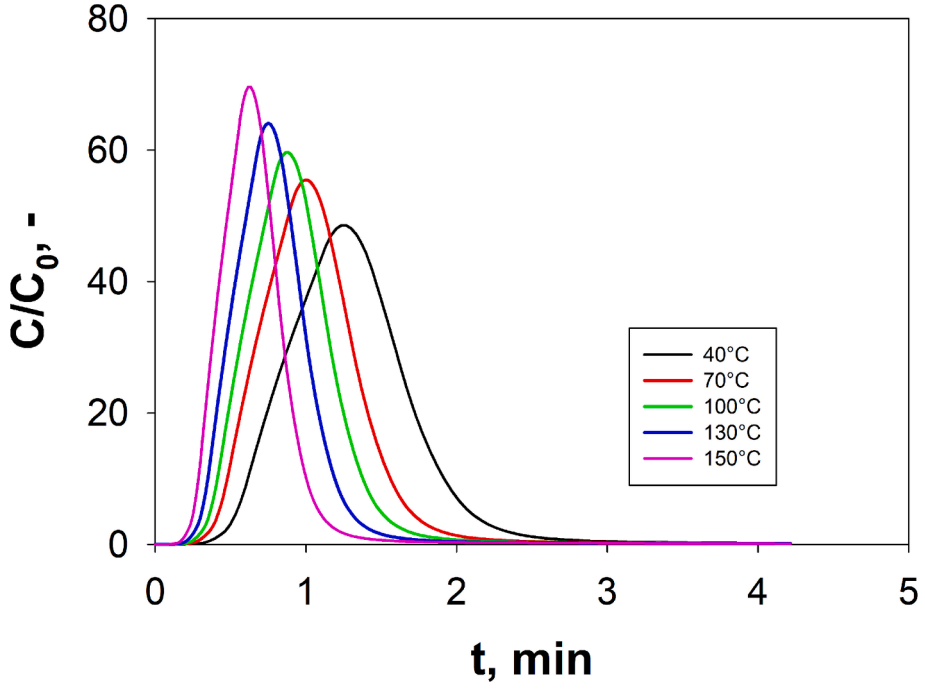


Fig. 11. CO_2 desorption profiles: CO_2 outlet concentration as function of time at different desorption temperatures. Adsorption step: T = 28 °C; C_0 = 15 %vol.

diffusivity of both N_2 and CO_2 molecules at elevated temperatures.

The CO_2 desorption profiles were further analyzed to evaluate desorption efficiency, which was measured using three parameters: CO_2 recovery level (R), desorption process duration at a specific recovery level (t_d), and average CO_2 concentration in the desorbing stream (C_m). The recovery and CO_2 average concentration profiles as function of the desorption time are shown in Fig. 12a and b. The recovery curves clearly show that increasing the temperature significantly speeds up the desorption process (Fig. 12a).

At 150 °C, the recovery reaches nearly 100 % in less than 1 min, demonstrating relatively fast and efficient desorption. In contrast, at lower temperatures, such as 40 °C, the recovery process is much slower, taking around 3 min to reach completion. This trend suggests that higher temperatures provide increased thermal energy, which accelerates CO_2 desorption by breaking the bonds between CO_2 molecules and CALF-20 surface more easily. This results in faster recovery and higher desorption rates. The recovery curves at higher temperatures (T > 100 °C) tend to come closer as temperature increases, which indicates that, beyond a certain temperature, the recovery process becomes less sensitive to further increases in temperature. When the desorption time is set at 1 min, the recovery rate is approximately 50 % at 70 °C, but it increases significantly to about 75 % when the temperature is increased to 100 °C. However, further increases in temperature lead to diminishing benefits in terms of recovery efficiency. The recovery level improves by only around 15 % (reaching roughly 90 %) as the temperature rises from 100 °C to 130 °C, and the gain is even less pronounced, about 7 %, when the temperature is further increased from 130 °C to 150 °C. This trend is further illustrated in Fig. 12c, which shows that desorption time, t_d, decreases with rising desorption temperatures for all selected recovery levels, ranging from 70 % to 95 %. Notably, the curves are steeper at lower temperatures (below 100 °C), indicating that increasing the temperature in this range leads to a more pronounced reduction in the time required to achieve the target recovery levels.

The outlet CO_2 concentration, C_m, exhibits a different behavior compared to the recovery, following a non-monotonic trend (Fig. 12b) driven by the interplay between the continued desorption of CO_2 and the dilution effect of the N_2 purge gas. Specifically, in the early stages of desorption, C_m rises sharply due to the rapid release of CO_2, particularly at higher temperatures like 150 °C and 130 °C, where desorption is most intense. This initial increase occurs because the CO_2 previously bound to the adsorbent is quickly released into the outlet stream. However, as desorption continues, the dynamics shift. The continuous flow of N_2 purge gas begins to dilute the concentration of CO_2 in the outlet stream. Although CO_2 is still being desorbed, the increasing presence of N_2 causes C_m to decrease as the ratio of N_2 to CO_2 in the recovered stream rises. Clearly, this dilution effect becomes more pronounced over time as the amount of CO_2 left on the adsorbent diminishes. With less CO_2 being released, the N_2 flow becomes the dominant factor in the outlet stream, further lowering Cm. Concerning the influence of desorption temperature, Fig. 12d illustrates that increasing temperatures positively affect the desorption process in terms of CO_2 purity. Specifically, at a given recovery level, C_m consistently increases as temperatures rise, which aligns with the observed heightened CO_2 release into the outlet stream when the process is performed at higher temperatures.

This analysis highlights the need to strike a balance between maximizing the CO_2 recovery level and maintaining CO_2 purity in the outlet stream. While larger desorption times boost recovery, they also increase the dilution of CO_2 by the N_2 purge gas, lowering purity. Likewise, the need also exists to balance maximizing CO_2 recovery effectiveness and maintaining efficiency in terms of energy consumption during the desorption process. As the results show, increasing the desorption temperature consistently benefits both CO_2 recovery (R) and the average outlet CO_2 concentration (C_m). Higher temperatures enhance the desorption rate, allowing more CO_2 to be released from the adsorbent in a shorter time, which increases both the recovery and the concentration of CO_2 in the outlet stream. This makes higher temperatures advantageous in terms of desorption performance, as they drive more efficient CO_2 release. However, the downside of increasing the desorption temperature lies in the associated energy demand. Higher temperatures require more energy input to heat the system, which could significantly impact the overall energy efficiency and cost of the process. Hence, while raising the temperature leads to faster desorption and higher recovery levels and outlet CO_2 concentrations, the energy required to sustain these elevated temperatures could diminish the economic and

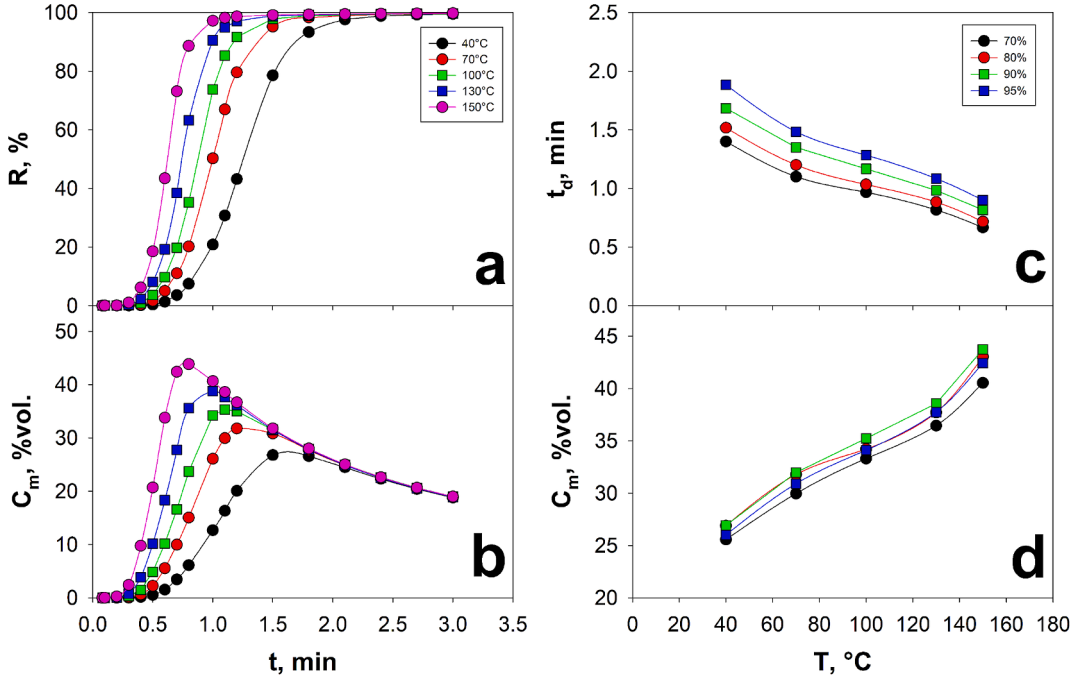


Fig. 12. CO_2 Recovery, R, (a) and mean outlet CO_2 concentration, C_m, (b) as functions of time at different desorption temperatures. Desorption time, t_d, (c) and mean outlet CO_2 concentration, C_m, (e) as functions of desorption temperature at different values of CO_2 Recovery. Adsorption step: T = 28 °C; C_0 = 15 %vol.

environmental benefits of the CO_2 capture process.

Therefore, optimizing desorption conditions is crucial to achieving both high CO_2 recovery and sufficient purity for effective downstream use, while also carefully managing the energy demand. Balancing these factors is key to ensuring the process overall efficiency and sustainability.

3.3.1. TSA cycles

Fig. 13a presents the CO_2 outlet profile during the cyclic adsorption/desorption tests performed on CALF-20 over 10 cycles. The repeating patterns suggest stable performance of CALF-20 across multiple cycles. The material appears to regenerate effectively during each desorption phase, which is crucial for industrial applications requiring long-term cycling stability.

Fig. 13b highlights the stability of key adsorption parameters over the 10 cycles. The plots for q_e, t_b, $\Delta\tau$, and ψ exhibit minimal variation across cycles, which further demonstrates CALF-20 ability to maintain consistent adsorption performance across multiple adsorption/desorption cycles.

This cyclic stability exhibited by CALF-20 is highly desirable for potential industrial-scale applications. Its ability to keep consistent CO_2 capture performance over multiple adsorption/desorption prevents the rapid degradation of capture capacity often occurring in such solid-based capture processes [6,13,15]. This durability minimizes the need for frequent make-up of fresh sorbent material. Consequently, this not only ensures reliable operation over long-term cycling but also enhances the sustainability and cost-effectiveness of the process, making it more efficient and economically viable for large-scale use.

It is noteworthy that, while this study was limited to ten cycles, literature data are available that investigate the cycling stability of CALF-20 over extended periods. Specifically, Lin et al. (2021) [21] demonstrated that CALF-20 retains its CO_2 adsorption capacity over 30 adsorption/desorption cycles under TSA conditions (desorption temperature of 150 °C), with no significant decline in adsorption capacity or structural integrity. Additionally, it is also important to highlight that CALF-20, as a physisorbent, benefits from the inherent stability of physisorption mechanisms, which involve weak and reversible interactions under mild regeneration conditions, minimizing risks of structural degradation. The regeneration protocol adopted in the present study, which operates at moderate desorption temperatures (< 150 °C), aligns with these principles and is designed to minimize stress on the sorbent material. Therefore, the stability of CALF-20, also synthesized via the proposed alternative mechanochemical approach, is expected to reliably persist beyond the 10 tested cycles.

4. Conclusions

This study demonstrated the effectiveness of CALF-20, a zinc-based metal–organic framework (MOF) synthesized via an unconventional mechanochemical approach, for CO_2 capture using temperature swing adsorption (TSA). The mechanochemical synthesis provides environmental and operational advantages, reducing solvent use and reaction time while maintaining the structural integrity essential for efficient CO_2 adsorption.

Thermodynamic and kinetic analyses underscore CALF-20 strong TSA performance. Sips isotherm analysis confirmed a high CO_2 adsorption capacity, reaching up to 2.55 mmol g^{-1} at 28 °C under a CO_2 partial pressure of 0.2 atm. Isosteric heat of adsorption values between 22–29 kJ mol^{-1} indicate physisorption as the primary mechanism. Kinetic studies identified the pseudo-first-order model as the best fit for CO_2 adsorption, further suggesting a process dominated by physical adsorption, which is advantageous for rapid adsorption and desorption cycles.

The desorption analysis highlights the importance of balancing high CO_2 recovery with maintaining CO_2 purity in the outlet stream. Elevated desorption temperatures significantly enhance CO_2 recovery rates and concentration in the outlet, a achieving nearly complete CO_2 recovery in under 1 min at 150 °C. However, these higher temperatures require more energy input, which can affect the overall efficiency and sustainability of the process. Besides, longer desorption times, while beneficial for recovery, can lead to increased dilution of CO_2 in the outlet due to the continuous N_2 purge gas flow, thereby reducing CO_2 purity. Thus, optimizing desorption conditions to maximize CO_2 recovery and purity while minimizing energy consumption is essential for making this approach viable in real applications.

While the obtained results highlight CALF-20 promising performance for CO_2 capture, addressing practical challenges remains a critical step toward ensuring its industrial deployment. In particular, ongoing efforts should focus on the following aspects:

- Mechanochemical synthesis scale-up – One of the key challenges lies in scaling up the mechanochemical synthesis process, which requires the optimization of various parameters to achieve consistent material properties at larger scales. For instance, the ball-to-powder ratio, milling speed, and liquid-assisted grinding conditions must be carefully calibrated to preserve the structural integrity and functional efficiency of CALF-20. These adjustments are essential to maintain the high adsorption performance observed in laboratory conditions while enabling economically feasible production at an industrial scale.
- Testing CALF-20 stability under industrially relevant conditions – Ensuring CALF-20 robustness in real-world applications necessitates evaluating its performance under industrially relevant conditions. This includes assessing the material behavior in the presence of humidity, a common challenge in flue gas environments, and its resistance to impurities such as SO_x and NO_x. These contaminants can potentially impact the adsorption efficiency and durability of the material over extended operational cycles. Stability studies under these conditions will provide valuable insights into the long-term

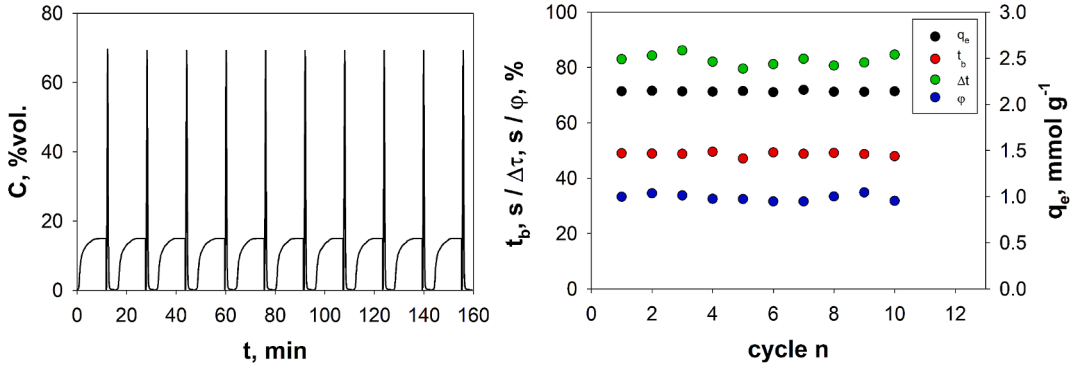


Fig. 13. A) tsa cycles. b) co_2 adsorption parameters as functions of the cycle number. Adsorption step: T = 28 °C; C_0 = 15 %vol. Desorption step: T = 150 °C; C_0 = 0.

applicability of CALF-20 in flue gas treatment and other industrial CO_2 capture processes.

- Pilot-scale implementations – Future efforts should also focus on pilot-scale implementations of CALF-20 to assess its adsorption efficiency and regeneration performance during continuous operations. These studies will help identify potential operational issues, such as thermal stability, pressure drop in adsorption systems, and material attrition, which are critical for designing scalable and sustainable CO_2 capture systems. Together, these efforts will bridge the gap between laboratory-scale findings and real-world applications, paving the way for CALF-20 to become a viable and impactful material in industrial CO_2 capture technologies.

CRediT authorship contribution statement

Federica Raganati: Writing – review & editing, Writing – original draft, Methodology, Investigation, Conceptualization. **Mariangela Bellusci:** Writing – review & editing, Methodology, Investigation, Conceptualization. **Francesco Leardi:** Methodology, Investigation. **Francesca Varsano:** Writing – review & editing, Methodology, Investigation, Conceptualization. **Paola Ammendola:** Writing – review & editing, Methodology, Investigation, Conceptualization.

Declaration of competing interest

The authors declare that they have no known competing financial interests or personal relationships that could have appeared to influence the work reported in this paper.

Acknowledgement

This work was supported by MASE within the framework of the Accordo di Programma Ministero dell'Ambiente e della Sicurezza Energetica-ENEA, PTR2022–2024 Project 1.6 "Efficienza energetica dei prodotti e dei processi industriali.

Appendix A. Supplementary data

Supplementary data to this article can be found online at https://doi.org/10.1016/j.cej.2025.159966.

Data availability

No data was used for the research described in the article.

References

[1] H. Choi, S. Lee, S. Jeong, Y.K. Hong, S.Y. Kim, Synthesis and CO2 Capture of Porous Hydrogel Particles Consisting of Hyperbranched Poly(amidoamine)s, Gels 8 (2022) 500, https://doi.org/10.3390/gels8080500.

[2] C. Ortiz, S. García-Luna, R. Chacartegui, J.M. Valverde, L. Pérez-Maqueda, Partial oxycombustion-calcium looping hybridisation for CO2 capture in waste-to-energy power plants, J Clean Prod 403 (2023) 136776, https://doi.org/10.1016/j.jclepro.2023.136776.

[3] M.A. Murmura, A. Brasiello, Challenges and opportunities ofprocess intensification for the conversion of waste CO2 to liquid fuels, Chem. Eng. Process. - Process Intesif. 186 (2023) 109329, https://doi.org/10.1016/j.cep.2023.109329.

[4] P. Ammendola, R. Chirone, G. Ruoppolo, G. Russo, Production of hydrogen from thermo-catalytic decomposition of methane in a fluidized bed reactor, Chem. Eng. J. 154 (2009) 287–294, https://doi.org/10.1016/j.cej.2009.03.048.

[5] L.M. Romeo, D. Minguell, R. Shirmohammadi, J.M. Andrés, Comparative Analysis of the Efficiency Penalty in Power Plants of Different Amine-Based Solvents for CO2Capture, Ind Eng Chem Res 59 (2020) 10082–10092, https://doi.org/10.1021/ACS.IECR.0C01483/ASSET/IMAGES/LARGE/IE0C01483_0006.JPEG.

[6] F. Raganati, P. Ammendola, CO 2 Post-combustion Capture: A Critical Review of Current Technologies and Future Directions, Energy Fuel 38 (2024) 13858–13905, https://doi.org/10.1021/acs.energyfuels.4c02513.

[7] A. Samanta, A. Zhao, G.K.H. Shimizu, P. Sarkar, R. Gupta, Post-Combustion CO2 Capture Using Solid Sorbents: A Review, Ind. Eng. Chem. Res 51 (2012) 1438–1463, https://doi.org/10.1021/ie200686q.

[8] V. Scherer, D. Stolten, J. Franz, E. Riensche, CCS separation techniques - Review on existing technologies and developments, Chem Ing Tech 84 (2012) 1026–1040, https://doi.org/10.1002/cite.201100233.

[9] M.G. Plaza, S. García, F. Rubiera, J.J. Pis, C. Pevida, Post-combustion CO2 capture with a commercial activated carbon: Comparison of different regeneration strategies, Chem. Eng. J. 163 (2010) 41–47, https://doi.org/10.1016/j.cej.2010.07.030.

[10] M. Danish, V. Parthasarthy, M.K. Al Mesfer, CO2 capture using activated carbon synthesized from date stone: breakthrough, equilibrium, and mass-transfer zone, Carbon Letters 31 (2021) 1261–1272, https://doi.org/10.1007/s42823-021-00249-y.

[11] R. Girimonte, B. Formisani, F. Testa, Adsorption of CO2 on a confined fluidized bed of pelletized 13X zeolite, Powder Technol 311 (2017) 9–17, https://doi.org/10.1016/j.powtec.2017.01.033.

[12] R. Girimonte, F. Testa, M. Turano, G. Leone, M. Gallo, G. Golemme, Amine-Functionalized Mesoporous Silica Adsorbent for CO2 Capture in Confined-Fluidized Bed: Study of the Breakthrough Adsorption Curves as a Function of Several Operating Variables, Processes 10 (2022), https://doi.org/10.3390/pr10020422.

[13] M.K. Al Mesfer, V. Parthasarthy, M. Danish, M. Shah, K.B. Ansari, P. Ammendola, M.I. Khan, F. Raganati, A critical review on current progress and challenges in post-combustion CO 2 separation from flue gas, Sep Sci Technol 59 (2024) 1454–1476, https://doi.org/10.1080/01496395.2024.2377585.

[14] P. Ammendola, F. Raganati, R. Chirone, F. Miccio, Fixed bed adsorption as affected by thermodynamics and kinetics: Yellow tuff for CO2 capture, Powder Technol 373 (2020) 446–458, https://doi.org/10.1016/j.powtec.2020.06.075.

[15] F. Raganati, F. Miccio, P. Ammendola, Adsorption of Carbon Dioxide for Post-combustion Capture: A Review, Energy Fuel 35 (2021) 12845–12868, https://doi.org/10.1021/acs.energyfuels.1c01618.

[16] B. Chen, D. Fan, R.V. Pinto, I. Dovgaliuk, S. Nandi, D. Chakraborty, N. García-Moncada, A. Vimont, C.J. McMonagle, M. Bordonhos, A. Al Mohtar, I. Cornu, P. Florian, N. Heymans, M. Daturi, G. De Weireld, M. Pinto, F. Nouar, G. Maurin, G. Mouchaham, C. Serre, A Scalable Robust Microporous Al-MOF for Post-Combustion Carbon Capture, Adv. Sci. 11 (2024) 1–15, https://doi.org/10.1002/advs.202401070.

[17] M. Younas, M. Rezakazemi, M. Daud, M.B. Wazir, S. Ahmad, N. Ullah, S. R. Inamuddin, Recent progress and remaining challenges in post-combustion CO2 capture using metal-organic frameworks (MOFs), Prog Energy Combust Sci 80 (2020) 100849, https://doi.org/10.1016/j.pecs.2020.100849.

[18] R. Oktavian, R. Goeminne, L.T. Glasby, P. Song, R. Huynh, O.T. Qazvini, O. Ghaffari-Nik, N. Masoumifard, J.L. Cordiner, P. Hovington, V. Van Speybroeck, P.Z. Moghadam, Gas adsorption and framework flexibility of CALF-20 explored via experiments and simulations, Nat Commun 15 (2024) 1–10, https://doi.org/10.1038/s41467-024-48136-0.

[19] X. Wang, M. Alzayer, A.J. Shih, S. Bose, H. Xie, S.M. Vornholt, C.D. Malliakas, H. Alhashem, F. Joodaki, S. Marzouk, G. Xiong, M. Del Campo, P. Le Magueres, F. Formalik, D. Sengupta, K.B. Idrees, K. Ma, Y. Chen, K.O. Kirlikovali, T. Islamoglu, K.W. Chapman, R.Q. Snurr, O.K. Farha, Tailoring Hydrophobicity and Pore Environment in Physisorbents for Improved Carbon Dioxide Capture under High Humidity, J Am Chem Soc 146 (2024) 3943–3954, https://doi.org/10.1021/jacs.3c11671.

[20] C.-H. Ho, F. Paesani, Elucidating the Competitive Adsorption of H 2 O and CO 2 in CALF-20: New Insights for Enhanced Carbon Capture Metal–Organic Frameworks, ACS Appl Mater Interfaces 15 (2023) 48287–48295, https://doi.org/10.1021/acsami.3c11092.

[21] J. Bin Lin, T.T.T. Nguyen, R. Vaidhyanathan, J. Burner, J.M. Taylor, H. Durekova, F. Akhtar, R.K. Mah, O. Ghaffari-Nik, S. Marx, N. Fylstra, S.S. Iremonger, K. W. Dawson, P. Sarkar, P. Hovington, A. Rajendran, T.K. Woo, G.K.H. Shimizu, A scalable metal-organic framework as a durable physisorbent for carbon dioxide capture, Science 374 (2021) (1979) 1464–1469, https://doi.org/10.1126/science.abi7281.

[22] T.T.T. Nguyen, J. Bin Lin, G.K.H. Shimizu, A. Rajendran, Separation of CO2 and N2 on a hydrophobic metal organic framework CALF-20, Chemical Engineering Journal 442 (2022) 136263, https://doi.org/10.1016/J.CEJ.2022.136263.

[23] Y. Higuchi, M. Sugita, S. Moriya, T. Takewaki, S. Tanaka, Rapid synthesis of metal-organic framework CALF-20 in H2O/methanol solution under room temperature and normal pressure, Microporous Mesoporous Mater. 374 (2024) 113137, https://doi.org/10.1016/j.micromeso.2024.113137.

[24] T.T.T. Nguyen, B.M. Balasubramaniam, N. Fylstra, R.P.S. Huynh, G.K.H. Shimizu, A. Rajendran, Competitive CO 2 /H 2 O Adsorption on CALF-20, Ind Eng Chem Res 63 (2024) 3265–3281, https://doi.org/10.1021/acs.iecr.3c04266.

[25] P. Ammendola, F. Raganati, R. Chirone, CO2 adsorption on a fine activated carbon in a sound assisted fluidized bed: Thermodynamics and kinetics, Chem. Eng. J. 322 (2017) 302–313, https://doi.org/10.1016/j.cej.2017.04.037.

[26] F. Raganati, M. Alfe, V. Gargiulo, R. Chirone, P. Ammendola, Isotherms and thermodynamics of CO2 adsorption on a novel carbon-magnetite composite sorbent, Chem. Eng. Res. Des. 134 (2018) 540–552, https://doi.org/10.1016/j.cherd.2018.04.037.

[27] T. Friščić, S.L. Childs, S.A.A. Rizvi, W. Jones, The role of solvent in mechanochemical and sonochemical cocrystal formation: a solubility-based approach for predicting cocrystallisation outcome, CrstEngComm 11 (2009) 418–426, https://doi.org/10.1039/B815174A.

[28] C. Espro, D. Rodríguez-Padrón, Re-thinking organic synthesis: Mechanochemistry as a greener approach, Curr Opin Green Sustain Chem 30 (2021) 100478, https://doi.org/10.1016/j.cogsc.2021.100478.

[29] E. Colacino, F. García, Mechanochemistry and Emerging Technologies for Sustainable Chemical Manufacturing, CRC Press, Boca Raton (2023), https://doi.org/10.1201/9781003178187.
[30] C.C. Obi, J.T. Nwabanne, P.K. Igbokwe, C.I. Idumah, V.U. Okpechi, H.C. Oyeoka, Novel advances in synthesis and catalytic applications of metal-organic frameworks - based nanocatalysts for CO2 capture and transformation, J Environ Chem Eng 12 (2024) 112835, https://doi.org/10.1016/j.jece.2024.112835.
[31] M. Pilloni, F. Padella, G. Ennas, S. Lai, M. Bellusci, E. Rombi, F. Sini, M. Pentimalli, C. Delitala, A. Scano, V. Cabras, I. Ferino, Liquid-assisted mechanochemical synthesis of an iron carboxylate Metal Organic Framework and its evaluation in diesel fuel desulfurization, Microporous Mesoporous Mater. 213 (2015) 14–21, https://doi.org/10.1016/j.micromeso.2015.04.005.
[32] M. Bellusci, A. Masi, M. Albino, D. Peddis, M. Petrecca, C. Sangregorio, A. La Barbera, F. Varsano, Fe3O4@HKUST-1 magnetic composites by mechanochemical route for induction triggered release of carbon dioxide, Microporous Mesoporous Mater. 328 (2021) 111458, https://doi.org/10.1016/j.micromeso.2021.111458.
[33] D. Ozer, Mechanochemistry: A Power Tool for Green Synthesis, in: Advances in Green Synthesis, 2021: pp. 23–39. https://doi.org/10.1007/978-3-030-67884-5_2.
[34] J.W.M. Osterrieth, J. Rampersad, D. Madden, N. Rampal, L. Skoric, B. Connolly, M. D. Allendorf, V. Stavila, J.L. Snider, R. Ameloot, J. Marreiros, C. Ania, D. Azevedo, E. Vilarrasa-Garcia, B.F. Santos, X. Bu, Z. Chang, H. Bunzen, N.R. Champness, S. L. Griffin, B. Chen, R. Lin, B. Coasne, S. Cohen, J.C. Moreton, Y.J. Colón, L. Chen, R. Clowes, F. Coudert, Y. Cui, B. Hou, D.M. D'Alessandro, P.W. Doheny, M. Dincă, C. Sun, C. Doonan, M.T. Huxley, J.D. Evans, P. Falcaro, R. Ricco, O. Farha, K. B. Idrees, T. Islamoglu, P. Feng, H. Yang, R.S. Forgan, D. Bara, S. Furukawa, E. Sanchez, J. Gascon, S. Telalović, S.K. Ghosh, S. Mukherjee, M.R. Hill, M. M. Sadiq, P. Horcajada, P. Salcedo-Abraira, K. Kaneko, R. Kukobat, J. Kenvin, S. Keskin, S. Kitagawa, K. Otake, R.P. Lively, S.J.A. DeWitt, P. Llewellyn, B. V. Lotsch, S.T. Emmerling, A.M. Pütz, C. Martí-Gastaldo, N.M. Padial, J. García-Martínez, N. Linares, D. Maspoch, J.A. Suárez del Pino, P. Moghadam, R. Oktavian, R.E. Morris, P.S. Wheatley, J. Navarro, C. Petit, D. Danaci, M.J. Rosseinsky, A. P. Katsoulidis, M. Schröder, X. Han, S. Yang, C. Serre, G. Mouchaham, D.S. Sholl, R. Thyagarajan, D. Siderius, R.Q. Snurr, R.B. Goncalves, S. Telfer, S.J. Lee, V. P. Ting, J.L. Rowlandson, T. Uemura, T. Iiyuka, M.A. van der Veen, D. Rega, V. Van Speybroeck, S.M.J. Rogge, A. Lamaire, K.S. Walton, L.W. Bingel, S. Wuttke, J. Andreo, O. Yaghi, B. Zhang, C.T. Yavuz, T.S. Nguyen, F. Zamora, C. Montoro, H. Zhou, A. Kirchon, D. Fairen-Jimenez, How Reproducible are Surface Areas Calculated from the BET Equation? Adv. Mater. 34 (2022) 2201502, https://doi.org/10.1002/adma.202201502.
[35] J. a. Mason, K. Sumida, Z.R. Herm, R. Krishna, Jeffrey.R. Long, Evaluating metal–organic frameworks for post-combustion carbon dioxide capture via temperature swing adsorption, Energy Environ Sci 4 (2011) 3030–3040. https://doi.org/10.1039/c1ee01720a.
[36] H.M. Kvamsdal, G. Haugen, H.F. Svendsen, Flue-gas cooling in post-combustion capture plants, Chem. Eng. Res. Des. 89 (2011) 1544–1552, https://doi.org/10.1016/j.cherd.2011.02.029.
[37] M.V. Gil, N. Álvarez-Gutiérrez, M. Martínez, F. Rubiera, C. Pevida, A. Morán, Carbon adsorbents for CO2 capture from bio-hydrogen and biogas streams: Breakthrough adsorption study, Chem. Eng. J. 269 (2015) 148–158, https://doi.org/10.1016/j.cej.2015.01.100.
[38] F. Raganati, M. Alfe, V. Gargiulo, R. Chirone, P. Ammendola, Kinetic study and breakthrough analysis of the hybrid physical/chemical CO2 adsorption/desorption behavior of a magnetite-based sorbent, Chem. Eng. J. 372 (2019) 526–535, https://doi.org/10.1016/j.cej.2019.04.165.
[39] R. Sips, On the Structure of a Catalyst Surface, J Chem Phys 16 (1948) 490–495, https://doi.org/10.1063/1.1746922.
[40] M. Saleh Shafeeyan, W. Mohd Ashri Wan Daud, A. Shamiri, N. Aghamohammadi, Adsorption equilibrium of carbon dioxide on ammonia-modified activated carbon, Chemical Engineering Research and Design 104 (2015) 42–52. https://doi.org/10.1016/j.cherd.2015.07.018.
[41] J. Sreńscek-Nazzal, U. Narkiewicz, A.W. Morawski, R. Wróbel, A. Gęsikiewicz-Puchalska, B. Michalkiewicz, Modification of Commercial Activated Carbons for CO 2 Adsorption, Acta Phys Pol A 129 (2016) 394–401. https://doi.org/10.12693/APhysPolA.129.394.
[42] D. Iruretagoyena Ferrer, Supported Layered Double Hydroxides as CO2 Adsorbents for Sorption-enhanced H2 Production, Springer International Publishing, Cham, 2016. https://doi.org/10.1007/978-3-319-41276-4.
[43] S.-C. Hsu, C. Lu, F. Su, W. Zeng, W. Chen, Thermodynamics and regeneration studies of CO2 adsorption on multiwalled carbon nanotubes, Chem Eng Sci 65 (2010) 1354–1361, https://doi.org/10.1016/j.ces.2009.10.005.
[44] F. Raganati, F. Miccio, G. Iervolino, E. Papa, P. Ammendola, Waste-derived tuff for CO2 Capture: Enhanced CO2 adsorption performances by Cation-Exchange tailoring, J. Ind. Eng. Chem. 138 (2024) 153–164, https://doi.org/10.1016/j.jiec.2024.03.049.
[45] S. Loganathan, M. Tikmani, S. Edubilli, A. Mishra, A.K. Ghoshal, CO2 adsorption kinetics on mesoporous silica under wide range of pressure and temperature, Chem. Eng. J. 256 (2014) 1–8, https://doi.org/10.1016/j.cej.2014.06.091.
[46] R. Serna-Guerrero, A. Sayari, Modeling adsorption of CO2 on amine-functionalized mesoporous silica. 2: Kinetics and breakthrough curves, Chemical Engineering Journal 161 (2010) 182–190, https://doi.org/10.1016/j.cej.2010.04.042.
[47] N. Álvarez-Gutiérrez, M.V. Gil, F. Rubiera, C. Pevida, Kinetics of CO2 adsorption on cherry stone-based carbons in CO2/CH4 separations, Chem. Eng. J. 307 (2017) 249–257, https://doi.org/10.1016/j.cej.2016.08.077.
[48] C. Goel, H. Kaur, H. Bhunia, P.K. Bajpai, Carbon dioxide adsorption on nitrogen enriched carbon adsorbents: Experimental, kinetics, isothermal and thermodynamic studies, J. CO2 Util. 16 (2016) 50–63, https://doi.org/10.1016/j.jcou.2016.06.002.
[49] S.Y. Lagergren, Zur Theorie der sogenannten Adsorption gelöster Stoffe, Kungliga Svenska Vetenskapsakad. Handlingar 24 (1898) 1–39.
[50] G. Blanchard, M. Maunaye, G. Martin, Removal of heavy metals from waters by means of natural zeolites, Water Res 18 (1984) 1501–1507, https://doi.org/10.1016/0043-1354(84)90124-6.
[51] Y.S. Ho, G. McKay, Kinetic model for lead(II) sorption on to peat, Adsorpt. Sci. Technol. (1998), https://doi.org/10.1177/026361749801600401.
[52] Y.S. Ho, G. McKay, A Comparison of Chemisorption Kinetic Models Applied to Pollutant Removal on Various Sorbents, Process Saf. Environ. Prot. 76 (1998) 332–340, https://doi.org/10.1205/095758298529696.
[53] M.A. Hubbe, S. Azizian, S. Douven, Implications of Apparent Pseudo-Second-Order Adsorption Kinetics onto Cellulosic Materials: A Review, BioResource 14 (2019) 7582–7626.
[54] G. Song, X. Zhu, R. Chen, Q. Liao, Y.-D. Ding, L. Chen, An investigation of CO2 adsorption kinetics on porous magnesium oxide, Chem. Eng. J. 283 (2016) 175–183, https://doi.org/10.1016/j.cej.2015.07.055.
[55] M. Karimi, A.E. Rodrigues, J.A.C. Silva, Designing a simple volumetric apparatus for measuring gas adsorption equilibria and kinetics of sorption. Application and validation for CO2, CH4 and N2 adsorption in binder-free beads of 4A zeolite, Chemical Engineering Journal 425 (2021) 130538, https://doi.org/10.1016/j.cej.2021.130538.
[56] H.N. Tran, S.-J. You, H.-P. Chao, Thermodynamic parameters of cadmium adsorption onto orange peel calculated from various methods: A comparison study, J Environ Chem Eng 4 (2016) 2671–2682, https://doi.org/10.1016/j.jece.2016.05.009.
[57] M. Pentimalli, M. Bellusci, F. Padella, High-Energy Ball Milling as a General Tool for Nanomaterials Synthesis and Processing, Handbook of Mechanical Nanostructuring (2015), https://doi.org/10.1002/9783527674947.ch28.
[58] X. Zhou, H. Yi, X. Tang, H. Deng, H. Liu, Thermodynamics for the adsorption of SO2, NO and CO2 from flue gas on activated carbon fiber, Chem. Eng. J. 200–202 (2012) 399–404, https://doi.org/10.1016/j.cej.2012.06.013.
[59] D.M. Ruthven, Principles of adsorption and adsorption processes, John Wiley & Sons, 1984.
[60] F. Raganati, V. Gargiulo, P. Ammendola, M. Alfe, R. Chirone, CO2 capture performance of HKUST-1 in a sound assisted fluidized bed, Chem. Eng. J. 239 (2014) 75–86, https://doi.org/10.1016/j.cej.2013.11.005.
[61] L. Bastin, P.S. Bárcia, E.J. Hurtado, J.A.C. Silva, A.E. Rodrigues, B. Chen, A Microporous Metal−Organic Framework for Separation of CO 2 /N 2 and CO 2 /CH 4 by Fixed-Bed Adsorption, J. Phys. Chem. C 112 (2008) 1575–1581, https://doi.org/10.1021/jp077618g.
[62] a O. Yazaydin, R.Q. Snurr, T.-H. Park, K. Koh, J. Liu, M.D. Levan, A.I. Benin, P. Jakubczak, M. Lanuza, D.B. Galloway, J.J. Low, R.R. Willis, Screening of metal-organic frameworks for carbon dioxide capture from flue gas using a combined experimental and modeling approach., J Am Chem Soc 131 (2009) 18198–9. https://doi.org/10.1021/ja9057234.
[63] A.R. Millward, O.M. Yaghi, Metal−Organic Frameworks with Exceptionally High Capacity for Storage of Carbon Dioxide at Room Temperature, J Am Chem Soc 127 (2005) 17998–17999, https://doi.org/10.1021/ja0570032.
[64] M. Arjmandi, M. Pakizeh, AN EXPERIMENTAL STUDY OF H2 AND CO2 ADSORPTION BEHAVIOR OF C-MOF-5 AND T-MOF-5: A COMPLEMENTARY STUDY, Braz. J. Chem. Eng. 33 (2016) 225–233, https://doi.org/10.1590/0104-6632.20160331s20140134.
[65] H.R. Abid, Z.H. Rada, L. Liu, S. Wang, S. Liu, Striking CO2 capture and CO2/N2 separation by Mn/Al bimetallic MIL-53, Polyhedron 193 (2021) 114898, https://doi.org/10.1016/j.poly.2020.114898.
[66] B.C.R. Camacho, R.P.P.L. Ribeiro, I.A.A.C. Esteves, J.P.B. Mota, Adsorption equilibrium of carbon dioxide and nitrogen on the MIL-53(Al) metal organic framework, Sep Purif Technol 141 (2015) 150–159, https://doi.org/10.1016/j.seppur.2014.11.040.
[67] Y. Park, D.-K. Moon, Y.-H. Kim, H. Ahn, C.-H. Lee, Adsorption isotherms of CO2, CO, N2, CH4, Ar and H2 on activated carbon and zeolite LiX up to 1.0 MPa, Adsorption 20 (2014) 631–647, https://doi.org/10.1007/s10450-014-9608-x.
[68] M. Wei, Q. Yu, W. Duan, L. Hou, K. Liu, Q. Qin, S. Liu, J. Dai, Equilibrium and Kinetics Analysis of CO 2 Adsorption on Waste Ion-exchange Resin-based Activated Carbon, J Taiwan Inst Chem Eng 77 (2017) 161–167, https://doi.org/10.1016/j.jtice.2017.04.040.
[69] M.F. Freundlich, Over the adsorption in solution, J Phys Chem 57 (1906) 355–471.
[70] J. Toth, State Equations of the Solid-Gas Interface Layers, Acta Chimica Academiae Scientiarum Hungaricae 69 (1971) 311–328.
[71] A. Heydari-Gorji, A. Sayari, CO2 capture on polyethylenimine-impregnated hydrophobic mesoporous silica: Experimental and kinetic modeling, Chem. Eng. J. 173 (2011) 72–79, https://doi.org/10.1016/j.cej.2011.07.038.
[72] D. Bahamon, L.F. Vega, Systematic evaluation of materials for post-combustion CO 2 capture in a Temperature Swing Adsorption process, Chem. Eng. J. 284 (2016) 438–447, https://doi.org/10.1016/j.cej.2015.08.098.
[73] S. Keskin, Molecular Simulations for Adsorption-Based CO2 Separation Using Metal Organic Frameworks, Metal-Organic Frameworks (2016), https://doi.org/10.5772/64226.
[74] V.K. Singh, E. Anil Kumar, Measurement and analysis of adsorption isotherms of CO2 on activated carbon, Appl Therm Eng 97 (2016) 77–86, https://doi.org/10.1016/j.applthermaleng.2015.10.052.
[75] K. Zhang, Z. Qiao, J. Jiang, Molecular design of zirconium tetrazolate metal-organic frameworks for CO2 capture, Cryst Growth Des 17 (2017) 543–549,

https://doi.org/10.1021/ACS.CGD.6B01405/SUPPL_FILE/CG6B01405_SI_001.PDF.
[76] A.L. Yaumi, M.Z.A. Bakar, B.H. Hameed, Recent advances in functionalized composite solid materials for carbon dioxide capture, Energy 124 (2017) 461–480, https://doi.org/10.1016/j.energy.2017.02.053.
[77] Y. Belmabkhout, A. Sayari, Effect of pore expansion and amine functionalization of mesoporous silica on CO2 adsorption over a wide range of conditions, Adsorption 15 (2009) 318–328, https://doi.org/10.1007/s10450-009-9185-6.
[78] A. Koide, T. Kihara, Intermolecular forces for D2, N2, O2, F2 and CO2, Chem Phys (1974), https://doi.org/10.1016/0301-0104(74)80004-2.
[79] S. Himeno, T. Tomita, K. Suzuki, S. Yoshida, Characterization and selectivity for methane and carbon dioxide adsorption on the all-silica DD3R zeolite, Microporous Mesoporous Mater. 98 (2007) 62–69, https://doi.org/10.1016/j.micromeso.2006.05.018.
[80] P. Ning, F. Li, H. Yi, X. Tang, J. Peng, Y. Li, D. He, H. Deng, Adsorption equilibrium of methane and carbon dioxide on microwave-activated carbon, Sep Purif Technol 98 (2012) 321–326, https://doi.org/10.1016/j.seppur.2012.07.001.
[81] J. Wang, X. Guo, Adsorption kinetic models: Physical meanings, applications, and solving methods, J Hazard Mater 390 (2020) 122156, https://doi.org/10.1016/j.jhazmat.2020.122156.
[82] Y. Guo, H. Zhang, Y. Liu, Desorption characteristics and kinetic parameters determination of molecular sieve by thermogravimetric analysis/differential thermogravimetric analysis technique, Adsorpt. Sci. Technol. 36 (2018) 1389–1404, https://doi.org/10.1177/0263617418772665.
[83] Y.-F. Huang, P.-T. Chiueh, C.-H. Shih, S.-L. Lo, L. Sun, Y. Zhong, C. Qiu, Microwave pyrolysis of rice straw to produce biochar as an adsorbent for CO2 capture, Energy 84 (2015) 75–82, https://doi.org/10.1016/j.energy.2015.02.026.
[84] M. Cinke, J. Li, C.W. Bauschlicher, A. Ricca, M. Meyyappan, CO2 adsorption in single-walled carbon nanotubes, Chem Phys Lett 376 (2003) 761–766, https://doi.org/10.1016/S0009-2614(03)01124-2.